UNIVERSITY OF OSLO

MASTER THESIS

Deterministic Prediction Of Sea Waves-Long Crested Sea

By:
Abushet SIMANESEW

Supervisor:
Prof. Karsten TRULSEN

A thesis submitted in fulfillment of the requirements
for the degree of Master of Science

in Fluid Mechanics

(Master i Anvendt matematikk og mekanikk)

Department of Mathematics
Faculty of Mathematics and Natural Sciences

May 2013

Matematisk Institutt
Det matematisk-naturvitenskapelige fakultet

UiO : Universitetet i Oslo

UNIVERSITY OF OSLO

Abstract

Faculty of Mathematics and Natural Sciences

Master of Science

Deterministic Prediction Of Sea Waves-Long Crested Sea

by Abushet Simanesew

The deterministic prediction of long crested sea waves has been investigated using linear and nonlinear propagation models. The linear model, derived from the linear wave theory, takes surface tension and viscous damping into account on arbitrarily deep water. The nonlinear model, derived from cubic Schrödinger equation, is implemented on deep water surface gravity waves. Experimental measurements of surface elevation have been used to initialize the simulation and control the accuracy of the prediction. Outliers and missing data are appropriately handled before doing any simulation. Comparisons between theoretically predicted and experimentally measured surface elevations are presented for different probe locations downstream of the wave tank. In the study, energy density is used as the norm to calculate the prediction error. The prediction error, both in space and space-time have been computed in each of the model used. The space-time prediction error is finally used as a basis to investigate the key parameter bounding the prediction region. Based on the results from the two models, group velocity corresponding to the peak spectrum is found to be the relevant parameter that bounds the prediction region.

Acknowledgements

I am deeply indebted to my supervisor professor Karsten Trulsen. Without his guidance, support and comments, I would never have been accomplished my thesis. His willingness, engagement and the methods he used to discuss issues that arose at every step of the study have helped me to understand and implement the theoretical background on the deterministic prediction of sea waves.

Then my thanks goes to Tore Magnus Arnesen Taklo, for his willingness to make available his experimental measurements. My thanks also goes to the department, especially to the professors, for giving me a solid background on the theories behind the subject of my thesis.

Finally, I would like to thank my fellow students, studying and sharing comments with them have helped me much. And most importantly, I would like to send my thanks to all my friends who helped me during the work of my thesis.

Contents

List of Figures

List of Tables

Abbreviations

DSWP	**D**eterministic **S**ea **W**ave **P**redictioin
NLS	**N**on**L**inear **S**chrödinger
MNLS	**M**odified **N**on**L**inear **S**chrödinger

Physical Constants

Gravitational acceleration $g \approx 9.81\ \mathrm{ms}^{-2}$

Symbols

H	sea bottom depth	m
a	amplitude	m
p	pressure	Pascal
t	time	s
T	period	s
T_c	characteristic period	s
f	frequency	Hz
u	horizontal velocity component	ms^{-1}
w	vertical velocity component	ms^{-1}
k	wavenumber	m^{-1}
c	phase speed	ms^{-1}
$\mathbf{c_g}$	group velocity	ms^{-1}
$\mathbf{c_{gP}}$	group velocity corresponding to the peak spectrum	ms^{-1}
$\mathbf{c_{gH}}$	the slowest group velocity	ms^{-1}
$\mathbf{c_{gL}}$	the fastest group velocity	ms^{-1}
k_c	wavenumber corresponding to characteristic frequency	m^{-1}
a_c	characteristic amplitude	m
k_p	wavenumber corresponding ω_p	m^{-1}
a_p	peak amplitude	m
A, A_2 and A_3	first, second and third harmonic complex amplitudes for ϕ	m^2s^{-1}
B, B_2 and B_3	first, second and third harmonic complex amplitudes for η	m
η	surface elevation	m
ϕ	velocity potential	m^2s^{-1}
$\bar{\eta}$	mean surface elevation	m

$\bar{\phi}$	mean velocity potential	$\mathrm{m^2s^{-1}}$
ω	angular frequency	$\mathrm{rads^{-1}}$
λ	wavelength	m
σ	surface tension	$\mathrm{Nm^{-1}}$
ρ	density	$\mathrm{kgm^{-3}}$
ν	coefficient of kinematic viscosity	$\mathrm{m^2s^{-1}}$
ω_c	characteristic frequency	$\mathrm{rads^{-1}}$
ω_p	peak frequency	$\mathrm{rads^{-1}}$
ϵ	characteristic steepness	

Chapter 1

Introduction

1.1 Short introduction

FIGURE 1.1: Typical marine operations.

Fishing activities and hunting of sea mammals are examples of challenging marine operations in the early daily human activities. Transportation of cargo, naval warfare and various other activities were undertaken with better skills under hostile environment. Offshore activities and human skills got better over years without much knowledge of mathematics, mechanics and dynamics. This has cost much in terms of life and economy. Today, offshore industry becomes a day to day human activity with improved knowledge of mathematics to forecast the sea state and design enhanced offshore technology which match the environment.

Statistical forecasting plays a vital role in predicting the sea state conditions before hand and enables offshore industry to undergo marine activities [1]. However such statistical results may not give the real time sea state for critical marine operations such as lifting equipment off transportation barge deck, helicopter operations, landing of subsea module into a template and jacket platform installation. Figure 1.1 is taken from the course MEK4450 (DNV kværner module) [2] given at UIO. The figure summarizes some of typical marine operations which require deterministic forecasting of real time sea state to calculate the real time vessel motion including in an unforeseen environment [3]. Much work has been done on the deterministic wave prediction of both short- and long-crested waves to improve the prediction region both in space and time.

The thesis presents a study on the precision and key parameter bounding the prediction region applying linear- and nonlinear long- and short-crested wave propagation models. The study on the long crested wave models are based upon experimentally measured long-crested surface elevation at UIO Fluid Mechanics division laboratory. The measurements are taken by Tore Magnus Arnesen Taklo for his ongoing Ph.D. thesis. Much work has been done on long-crested waves [1, 3–6]. The measured surface elevation data from the Laboratory are quite good both in space and time. Taking the advantage of the quality of experimentally measured wave data, it will be interesting to study the accuracy and key parameters bounding the prediction region. The study on short-crested wave models are based upon measurements of short-crested sea waves from MARIN. Until now very little analysis of measured short crested waves is done in terms of deterministic prediction of short-crested waves. Previously, several methods were analyzed which do not conform with the simple and effective nonlinear propagation models [7]. Due to short time available, the study on short-crested waves is not covered in this thesis.

Edgar *et al.* [1] have studied "*the effects of parameters on the maximum prediction time possible in short term forecasting of the sea surface shape*". One of the parameters is frequency component of the characteristic wave. The highest and lowest frequency components contained in the characteristic input trace determines the boundary lines of the prediction region [8]. However contradicting works have been published. The newly published works of Belmont *et al.* [9] argue that the prediction area for deterministic prediction can be bounded by lines, with a slope equal to the phase speed of the input trace instead of the group velocity. This may be difficult to accept in the classical theory of hydrodynamic wave theory. In this thesis, we will show the relevant velocity which bound the prediction area is the group velocity. The thesis argues that, the relevant velocity which bound the prediction area depends on the norm used to calculate the prediction error. The most obvious type of norm used in the paper is closely related to the energy density which would favor the group velocity as the relevant velocity bounding the prediction region.

1.2 Research Question

In this thesis, the reader may expect answers to the following main points:

- Deterministic prediction of surface elevation using linear model (linear wave theory) and comparison with experimental measurements.
- Deterministic prediction of surface elevation using nonlinear model (NLS equation) and comparison with experimental measurements.
- Prediction error of surface elevation in using linear model and nonlinear model.
- The key parameter bounding the prediction region.

1.3 Outline

In Chapter 2, the mathematical formulations of the theories behind the models used in this thesis will be presented. It is comprised of linear and nonlinear wave theory. In the linear theory, both surface tension and viscous damping are made included. In the linear part, relation between energy density and surface elevation and with group velocity is introduced. The nonlinear part provides summaries of the nonlinear Schrödinger equations both for short- and long-crested waves.

In Chapter 3, the preparation of input raw data and Fourier analysis is presented. The first part will present the experimental arrangement, the criteria used in removing outliers and NaNs and interpolation methods. In the second part, descretization and formulas for discrete Fourier transform and its inverse will be summarized before closing the chapter.

In Chapter 4, derivations of the linear and nonlinear models from the theories in Chapter 2 is presented. For each result displayed in the chapter, the steps will be discussed. The linear part is comprised of smoothing and characterization of the time series, deterministic forecast, criterion for deterministic prediction error and results. The nonlinear part is comprised of initialization, derivation of the nonlinear model from NLS equation, deterministic prediction and prediction error results.

In Chapter 5, a brief discussion on input data preparation and mainly on the results achieved in Chapter 4 will be summarized.

In Chapter 6, a short summary and conclusion of the results achieved will be covered. Finally, further work will be suggested before closing the chapter and the study.

In Appendices A, B and C, derivations, methods and figures which are not included in the main chapters will be provided.

Chapter 2

Wave Theory

In this chapter, the theory and mathematical formulations behind the linear and non-linear models (used in the deterministic prediction of sea waves) will be presented. The content of the chapter is less general than the stated subject, wave theory. Thus this chapter gives an overview of the mathematical formulations related to the thesis.

2.1 Linear theory

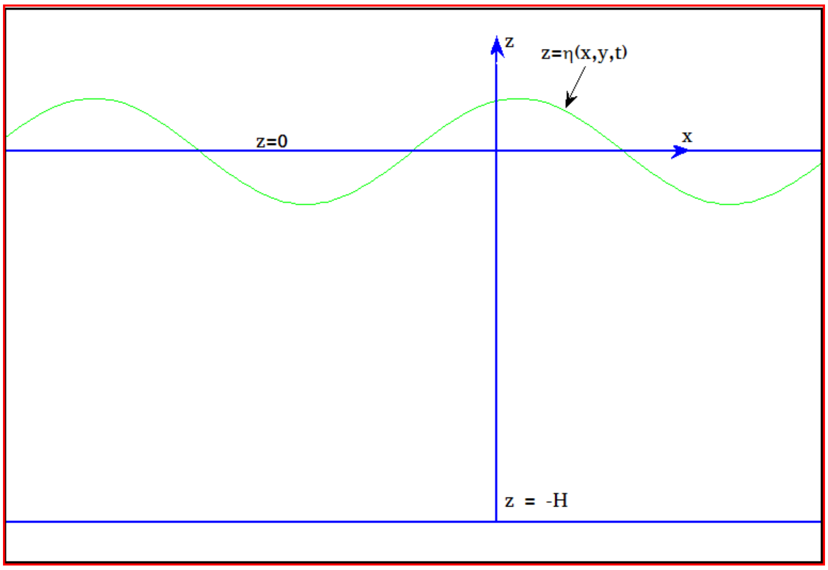

FIGURE 2.1: Two dimensional wave.

Consider a two-dimensional xz-plane surface waves in a homogeneous, incompressible, and frictionless fluid, overlaying in a horizontal flat sea bottom of depth H, as depicted in figure (2.1). The surface elevation is denoted as $\eta(x, t)$. Assuming the motion in the fluid is irrotational, there exists a velocity potential $\phi(x, z, t)$ so that the velocity field can be expressed in terms of the gradient of the potential. Following the compressibility of the fluid, the continuity equation yields

$$\nabla^2\phi = 0 \quad for \quad -H < z < \eta. \tag{2.1}$$

For surface waves the kinematic and dynamic boundary conditions at the free surface of the fluid respectively can be written as

$$\begin{array}{c} \frac{\partial\eta}{\partial t} + \nabla\phi\cdot\nabla\eta = \frac{\partial\phi}{\partial z} \\ \frac{\partial\phi}{\partial t} + \frac{1}{2}\nabla\phi\cdot\nabla\phi + \frac{p}{\rho} + g\eta = 0 \end{array} \quad at \quad z = \eta. \tag{2.2}$$

Due to the effect of surface tension, the pressure at the free surface is approximated as

$$p = -\sigma\frac{\partial^2\eta}{\partial x^2} \quad at \quad z = \eta. \tag{2.3}$$

In (2.3) the effect of atmospheric pressure is negelected. The kinematic boundary condition at sea floor is

$$\frac{\partial\phi}{\partial z} = 0 \quad at \quad z = -H. \tag{2.4}$$

For small amplitude, negelecting the nonlinear terms in (2.1) to (2.4), the linearized version of the boundary value problem is presented below.

The field equation to be solved is

$$\nabla^2\phi = 0 \quad for \quad -H < z < 0, \tag{2.5}$$

subject to the conditions at the boundaries

$$\frac{\partial\phi}{\partial t} - \frac{\sigma}{\rho}\frac{\partial^2\eta}{\partial x^2} + g\eta = 0, \quad at \quad z = 0, \tag{2.6}$$

$$\frac{\partial\eta}{\partial t} = \frac{\partial\phi}{\partial z} \quad at \quad z = 0, \tag{2.7}$$

$$\frac{\partial\phi}{\partial z} = 0, \quad at \quad z = -H. \tag{2.8}$$

The linear dynamic and kinematic boundary conditions (2.6) and (2.7) can be combined to get

$$\frac{\partial^2\phi}{\partial t^2} + g\frac{\partial\phi}{\partial z} - \frac{\sigma}{\rho}\left(\frac{\partial^2}{\partial x^2}\right)\frac{\partial\phi}{\partial z} = 0, \quad at \quad z = 0, \tag{2.9}$$

where g is the gravitational acceleration acting in the negative z direction. Equation 2.3 has been used to achieve equation 2.6. Note that the effect of surface tension is included in the boundary value problem. Its effect can be seen in the dynamic boundary condition (2.6).

"An arbitrary disturbance can be decomposed into various sinusoidal components by Fourier analysis, and the response of the system to an arbitrary small disturbance is the sum of the responses to the various sinusoidal componests", Kundu Cohen (2008)[8].

To solve the boundary value problem, we need to assume the form of the surface elevation $\eta(x,t)$. For example see equation 2.10 for a cosine dependence of η. Once the surface elevation assumed, the velocity potential $\phi(x,z,t)$ can be computed from the boundary value problem. The cosine dependence of η and the boundary conditions 2.6 and 2.8 indicate that the velocity potential ϕ is a sine function. Thus the Laplace equation for the velocity potential can be solved by a method of separation of variables. The form of the solution of the Laplace equation is $\phi = f(z)\sin(kx - \omega t)$ and substitute it into equation (2.5) to get (2.11). The constants that pop-up in the general solution can be determined from the conditions 2.7 and 2.8. See Appendix A.1 for detailed derivation.

$$\eta = a\cos(kx - \omega t), \tag{2.10}$$

$$\phi = \frac{ag}{\omega}\left(1 + \frac{\sigma k^2}{g\rho}\right)\frac{\cosh k(z+H)}{\cosh kH}\sin(kx - \omega t), \tag{2.11}$$

where a is the amplitude of the wave, k is the wavenumber defined in terms of the wavelength λ as

$$k = \frac{2\pi}{\lambda}, \tag{2.12}$$

and ω is the angular frequency defined in terms of the period of the wave T as

$$\omega = \frac{2\pi}{T}. \tag{2.13}$$

The angular frequency and wavenumber are connected through the dispersion relation for the capillary-gravity waves. In deriving the dispersion relation 2.14, equations 2.6, 2.10 and 2.11 have been used. See Appendix A.1 for the derivation.

$$\omega = \sqrt{\left(gk + \frac{\sigma k^3}{\rho}\right) \tanh KH.} \tag{2.14}$$

The phase speed ($c = \frac{\omega}{k}$), is then

$$c = \sqrt{gH}\left(1 + \frac{\sigma k^2}{\rho}\right)^{\frac{1}{2}}\left(\frac{\tanh KH}{KH}\right)^{\frac{1}{2}}. \tag{2.15}$$

For $\frac{\sigma k^2}{\rho g} << 1$, the effect of surface tension in equation 2.15 is very small. Thus a limiting wavelength (λ_m) should be set to decide whether the surface tension can be neglected or not. The expression for the limiting wavelength is derived from the first bracket of equation 2.15 see [10].

$$\lambda_m = \left(\frac{\sigma}{\rho g}\right)^{\frac{1}{2}}. \tag{2.16}$$

Surface tension dominates for waves with $\lambda < \lambda_m$ and can be neglected for waves with $\lambda > \lambda_m$. For air-water interface at a temperature of $20°C$, the surface tension $\sigma = 0.074N/m$ for clean water. Kundu, Cohen (2008).

The dispersion relation (2.14) will be used in Chapter 4 in the linear simulation of surface elevation in space and time, so as to include the effect of surface tension in the propagation of the waves. The value $\sigma = 0.074N/m$ is used in the simulation.

2.1.1 Energy,

Energy in surface gravity wave consists of kinetic energy due to motion of the fluid and potential energy due to deformation of the free surface by surface tension and the force of gravity. Beneath a unit length of the free surface, the average kinetic energy density is

$$E_k = \frac{\rho}{2}\int_{-H}^{0}(u^2 + w^2)dz, \tag{2.17}$$

the time average of kinetic energy

$$\overline{E}_k = \frac{\rho}{2}\int_{-H}^{0}(\overline{u^2} + \overline{w^2})dz, \tag{2.18}$$

and the instantaneous potential energy is

$$E_p = \frac{1}{2}\rho g \eta^2 + \frac{1}{2}\sigma\eta_x^2, \tag{2.19}$$

the time average of the potential energy

$$\overline{E}_p = \frac{1}{2}\rho g \overline{\eta^2} + \frac{1}{2}\sigma\overline{\eta_x^2}. \tag{2.20}$$

After substitution of the velocity field (A.13) and (A.14) and surface elevation (2.10) into 2.18 and 2.20, the total energy per unit length will be

$$\overline{E} = \overline{E}_k + \overline{E}_p = \rho g \overline{\eta^2} + \frac{\sigma}{2}\overline{\eta_x^2} = \frac{\rho g a^2}{2}\left(1 + \frac{\sigma k^2}{\rho g}\right). \tag{2.21}$$

The average energy flux **F** per unit length along the wave is

$$\mathbf{F} = \overline{E}c_g, \tag{2.22}$$

where c_g is group velocity. It can be defined as the derivative of angular frequency with respect to the wavenumber

$$c_g = \frac{d\omega}{dk}, \tag{2.23}$$

then (2.14) in to (2.23) gives the group velocity for the capillary-gravity waves

$$c_g = \frac{c}{2}\left[\frac{1 + \frac{3\sigma k^2}{\rho g}}{1 + \frac{\sigma k^2}{\rho g}} + \frac{2kH}{\sinh 2kH}\right]. \tag{2.24}$$

2.1.2 Effect of Viscous Damping

As introduced in Chapter 1, the linear model takes into account the effect of surface tension and viscous damping. The effect of surface tension is already made included in the dispersion relation (2.14) for friction free motion. Here the effect of viscous damping (motion with friction) will be introduced. Most of the material used here is from Lecture Notes in Hydrodynamic wave theory [11] given at the University of Oslo.

Let us consider a two-dimensional plane wave, homogeneous and incompressible Newtonian fluid overlying over an infinitely deep sea bottom. The linearized Navier-Stokes equations for small amplitude are

$$\frac{\partial u}{\partial t} = -\frac{1}{\rho}\frac{\partial p}{\partial x} + \nu\left(\frac{\partial^2 u}{\partial x^2} + \frac{\partial^2 u}{\partial z^2}\right), \tag{2.25}$$

$$\frac{\partial w}{\partial t} = -\frac{1}{\rho}\frac{\partial p}{\partial z} - g + \nu\left(\frac{\partial^2 w}{\partial x^2} + \frac{\partial^2 w}{\partial z^2}\right), \tag{2.26}$$

and the continuity equation

$$\frac{\partial u}{\partial x} + \frac{\partial w}{\partial z} = 0. \tag{2.27}$$

In the equations above, ν is the coefficient of kinematic viscosity. The linearized boundary conditions at the free surface are

$$\begin{aligned} &\tfrac{\partial u}{\partial z} + \tfrac{\partial w}{\partial x} = 0, \\ &\tfrac{\partial \phi}{\partial t} + g\eta + 2\nu\tfrac{\partial w}{\partial z} - \tfrac{\sigma}{\rho}\tfrac{\partial^2}{\partial x^2} = 0 \quad \text{and} \\ &\tfrac{\partial \eta}{\partial t} = w. \end{aligned} \tag{2.28}$$

If a very short wavelengths are neglected, the real part of roots of the general solution can be simplified and the the surface elevation can be written as

$$\eta = ae^{-2\nu k^2 t}\cos(kx - \omega t). \tag{2.29}$$

Note that the dispersion relation (2.14) is still valid. Intermediate steps which are necessary to achieve the final result (2.29) are omitted here. The reader may refer to the compendium referred in the first paragraph of this section or Lamb [12] and [13, 14] for details.

Hereafter equation 2.29 for viscous damping along with the dispersion relation (2.14) will be used for linear model simulations. However the time series are recorded in time at different probes, positioned at some interval downstream of the wave tank. The timeseries at the first probe will initialize the simulation in the linear propagation of the waves downstream of the wave tank. Then the resulting wave elevations will be compared with the corresponding time series recorded at different probe positions. Therefore it is preferable to replace the time t in the damping term of equation 2.29 by downstream distance x appropriately. This is done by expressing t in terms of distance and velocity i.e $t = \frac{x}{c_g}$. Here, c_g is the group velocity contained in the time series recorded at $x = 0$. Physically, t is the time required for the wave group to cover the distance x. For perfectly long-crested waves, the final equation will be

$$\eta = ae^{-2\nu k^2 \frac{x}{c_g}} \cos(kx - \omega t). \tag{2.30}$$

Wave solutions like in (2.30) is a monochromatic wave. Superposition of such waves of different frequencies give a more general regular wave. J.N. Newman [15]

$$\eta(x,t) = \sum_n Re\left[A_n e^{-2\nu k_n^2 \frac{x}{c_g}} \exp\left(-ik_n x + i\omega_n t\right)\right], \tag{2.31}$$

where k_n and ω_n are wavenumber and frequency of the nth component of the wave respectively, whereas A_n is a complex amplitude of the nth wave component and it has different phase.

Equation 2.31 is for perfectly long-crested waves. The equation may be modified for short-crested waves [7].

2.2 Nonlinear theory

The choice of nonlinear model may come after knowing the characteristic values of surface elevation to be used as initialization of simulation. Specially the characteristic steepness is the determining parameter. The details of such computations may be referred in Chapter 4. The characteristic steepness is found to be small such that a weakly nonlinear model can be used to model the nonlinear propagation of the surface elevation Trulsen [4]. In the following, the effect of surface tension and viscous damping are neglected.

For incompressible fluid the continuity equation can be written as

$$\nabla \cdot \mathbf{V} = 0. \tag{2.32}$$

Assuming an inviscid and irrotational fluid overlying over an infinitely deep sea bottom, there exist a velocity potential such that the velocity field $\mathbf{V} = \nabla\phi$. The velocity field into (2.32) yields the field equation as

$$\nabla^2\phi = 0 \quad for \quad -\infty < z < \eta. \tag{2.33}$$

As defined earlier in Section 2.1 and assuming constant atmospheric pressure the non-linear kinematic and dynamic boundary conditions at the free surface of the fluid are respectively

$$\begin{array}{c} \frac{\partial\eta}{\partial t} + \nabla\phi\cdot\nabla\eta = \frac{\partial\phi}{\partial z}, \\ \frac{\partial\phi}{\partial t} + \frac{1}{2}\nabla\phi\cdot\nabla\phi + g\eta = 0, \end{array} \qquad at \quad z = \eta. \tag{2.34}$$

The kinematic boundary condition at bottom is

$$\frac{\partial\phi}{\partial z} = 0 \quad at \quad z = -\infty. \tag{2.35}$$

Referring to [4, 16–18], for slow evolution of a wave, the velocity potential and surface elevation can be written in terms of higher harmonics of the characteristic wave

$$\phi = \bar{\phi} + Re\left(Ae^{-i(k_c x - \omega_c t)} + A_2 e^{-2i(k_c x - \omega_c t)} + A_3 e^{-3i(k_c x - \omega_c t)} + \ldots\right), \tag{2.36}$$

$$\eta = \bar{\eta} + Re\left(Be^{-i(k_c x - \omega_c t)} + B_2 e^{-2i(k_c x - \omega_c t)} + B_3 e^{-3i(k_c x - \omega_c t)} + \ldots\right), \tag{2.37}$$

where $\bar{\phi}$ and $\bar{\eta}$ are the zeroth harmonic representing the mean flow and surface elevation respectively and are slowly varying real functions of space and time, A and B are the first harmonic complex amplitudes and are functions of wave steepness $\epsilon = k_c a_c$. A_n and B_n are the higher harmonic complex amplitudes and are functions of ϵ^n. In the references cited above, opposite sign is used in the exponents of equations 2.36 and 2.37.

The spatial evolution of the first harmonic complex amplitudes is given by the Nonlinear Schrödinger equation. In this thesis the NLS equation is given in terms of B (surface elevation).

2.2.1 Long-crested

The linear and nonlinear spatial evolution of long-crested waves were derived in Trulsen [4] and Dysthe [18]. The equations are summarized as follows.

The linear Schrödinger equation with exact linear dispersion for arbitrary broad bandwidth is given by

$$\frac{\partial B}{\partial x}+\frac{2k_c}{\omega_c}\frac{\partial B}{\partial t}+\frac{ik_c}{\omega_c}\frac{\partial^2 B}{\partial t^2}=0. \tag{2.38}$$

If the leading nonlinear effects are included, the nonlinear Schrödinger equation up to order ϵ^3 is

$$\frac{\partial B}{\partial x}+\frac{2k_c}{\omega_c}\frac{\partial B}{\partial t}+\frac{ik_c}{\omega_c}\frac{\partial^2 B}{\partial t^2}+ik_c^2|B|^2B=0, \tag{2.39}$$

the reconstruction is achieved with the first and second harmonic amplitudes. Here the second harmonic complex amplitude is

$$B_2=\frac{k_c}{2}B^2. \tag{2.40}$$

The modified nonlinear Schrödinger (MNLS) equation in terms of the first harmonic complex amplitude is summarized below.

$$\frac{\partial B}{\partial x}+\frac{2k_c}{\omega_c}\frac{\partial B}{\partial t}+\frac{ik_c}{\omega_c}\frac{\partial^2 B}{\partial t^2}+ik_c^2|B|^2B-\frac{8k_c^3}{\omega_c}|B|^2\frac{\partial B}{\partial t}-\frac{2k_c^3}{\omega_c}B^2\frac{\partial B^*}{\partial t}-\frac{4ik_c^3}{\omega_c^2}\frac{\partial\bar{\phi}}{\partial t}B=0 \quad \text{at} \quad z=0, \tag{2.41}$$

$$\frac{\partial\bar{\phi}}{\partial z}+k_c\frac{\partial}{\partial t}|B|^2=0 \qquad at \quad z=0, \tag{2.42}$$

$$\frac{4k_c^2}{\omega_c^2}\frac{\partial^2\bar{\phi}}{\partial t^2}+\frac{\partial^2\bar{\phi}}{\partial z^2}=0 \qquad \text{for} \quad -\infty<z<0, \tag{2.43}$$

$$\frac{\partial\bar{\phi}}{\partial z}=0 \qquad \text{for} \quad z=-\infty. \tag{2.44}$$

The terms in equation 2.37 are

$$\bar{\eta} = -\frac{k_c}{\omega_c^2}\frac{\partial\bar{\phi}}{\partial t}, \qquad B_2 = \frac{k_c}{2}B^2 + \frac{ik_c}{\omega_c}B\frac{\partial B}{\partial t} \quad \text{and} \quad B_3 = \frac{3k_c^2}{8}B^3. \tag{2.45}$$

2.2.2 Short crested waves

The linear and nonlinear spatial evolution of short crested waves are summarized from Trulsen *et al.* [16] and [19, 20]. The terms in (2.45) are still valid.

The linear Schrödinger equation with exact linear dispersion takes the form

$$\frac{\partial B}{\partial x} + \mathcal{L}(\partial_t, \partial_y)B = 0. \tag{2.46}$$

Assuming $\frac{|\Delta\mathbf{k}|}{k_c} = O(\epsilon), (k_cH)^{-1} = O(\epsilon)$, the cubic nonlinear Schrödinger (NLS) equation is

$$\frac{\partial B}{\partial x} + 2\frac{\partial B}{\partial t} + i\frac{\partial^2 B}{\partial t^2} - \frac{i}{2}\frac{\partial^2 B}{\partial y^2} + i|B|^2 B = 0, \tag{2.47}$$

and if the third-order reconstruction is included, the MNLS equation will be

$$\frac{\partial B}{\partial x} + 2\frac{\partial B}{\partial t} + i\frac{\partial^2 B}{\partial t^2} - \frac{i}{2}\frac{\partial^2 B}{\partial y^2} + i|B|^2 B - \frac{\partial^3 B}{\partial t\partial y^2} - 8|B|^2\frac{\partial B}{\partial t} - 2B^2\frac{\partial B^*}{\partial t} - 2i\frac{\partial\bar{\phi}}{\partial t}B = 0, \tag{2.48}$$

$$\frac{\partial\bar{\phi}}{\partial z} = -\frac{\partial}{\partial t}|B|^2 \qquad \text{at} \quad z = 0, \tag{2.49}$$

$$\nabla^2\bar{\phi} = 0 \qquad \text{for} \quad -\infty < z < 0, \tag{2.50}$$

$$\frac{\partial\bar{\phi}}{\partial z} = 0 \qquad \text{for} \quad z \to -\infty. \tag{2.51}$$

If 2.48 is represented by a pseudo-differential operator, it becomes

$$\frac{\partial B}{\partial x} + \mathcal{L}(\partial_t, \partial_y)B + i|B|^2 B - 8|B|^2\frac{\partial B}{\partial t} - 2B^2\frac{\partial B^*}{\partial t} - 2i\frac{\partial\bar{\phi}}{\partial t}B = 0, \tag{2.52}$$

where the operator $\mathcal{L}(\partial_t, \partial_y)$ is given by

$$\mathcal{L}(\partial_t, \partial_y) = -i \left\{ \left[(1 + i\partial_t)^4 + \partial_y^2 \right]^{\frac{1}{2}} - 1 \right\} . \tag{2.53}$$

Chapter 3

Input Data And Fourier Analysis

3.1 Input Data

For the prediction of the long-crested wave, the wave data was provided by Tore Magnus Arnese Taklo. The data has been taken at Applied Mathematics and Mechanics lab. for his ongoing Ph.D. thesis. The schematic diagram of the wave tank is referred from [21].

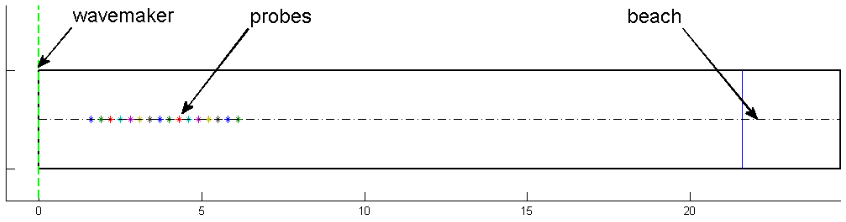

FIGURE 3.1: Schematic diagram of wave tank with probes (top view).

The data consists of sixteen probe measurements of surface elevation. The probes are located at equal distance along the wavetank as shown in figure 3.1. The first probe is 1.6 m away from the wavemaker whereas the sixteenth probe is 6.1 m away. The distance between two successive probes is 0.3 m and the distance between the first and the sixteenth is 4.5m. The data are sampled at frequency of $200 Hz$. In the raw data, measurements were missing for the largest and steepest waves. Part of a time series at the first probe showing the raw data is depicted in figure 3.2. Those missing data shall be filled with appropriate data. Handling of the missing data will be presented in the coming section.

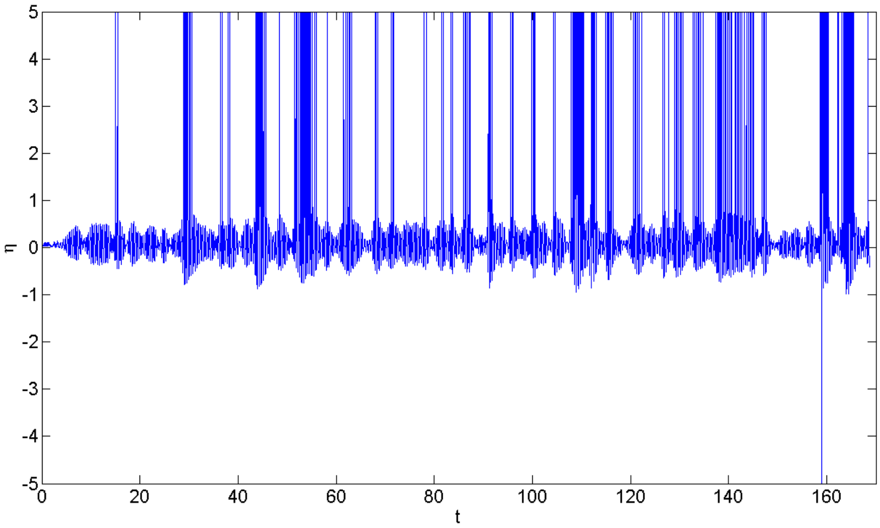

FIGURE 3.2: Typical raw data

3.1.1 Handling of outliers and missing data

The data holding NANs must be removed and replaced by interpolated data. This can be done by limiting upper and lower threshold. The choice of upper and lower thresholds depends on the heights of the generated waves and can also be limited by simple visual inspection. The application of upper and lower thresholds remove the spikes and introduce voided data points.

The upper and lower threshold are fixed to be $4cm$ and $-4cm$ respectively. These values are conservative compared to the respective highest crest and lowest trough found in the time series. The retained data can mathematically be expressed as

$$-4 < \eta_{i,j} < 4, \tag{3.1}$$

where $\eta_{i,j}$ is measured data, i and j are indices of the data points. The criterion (3.1) implies that, those values greater than or equal to $4cm$ and less than or equal to $-4cm$ will be removed. Apart from the spikes that appeared in the measured data, when one visually examines the data plot, some data points may appear to be dramatically far from the rest of the data. They may appear because of measurement error. Such values in the data may be called as outliers. After visual inspection and referring to [22] a value that is at least three times the standard deviation away from the mean is deemed as an outlier. Outliers shall be removed and replaced by an appropriate data. The removed outlier can mathematically be expressed as

$$|\eta_{i,j} - \bar{\eta}_j| > 3\sigma_j \tag{3.2}$$

where $\eta_{i,j}$ is measured data, $\bar{\eta}_j$ and σ_j are the mean and standard deviation of the data in each column.

After the spikes and outliers are successfully removed, the missing intermediate points in the data must be filled. In this case a cubic interpolation has been used to estimate the missing data representing the surface elevation. Figure 3.3 shows surface elevation measurements at sixteen probes after cubic interpolation.

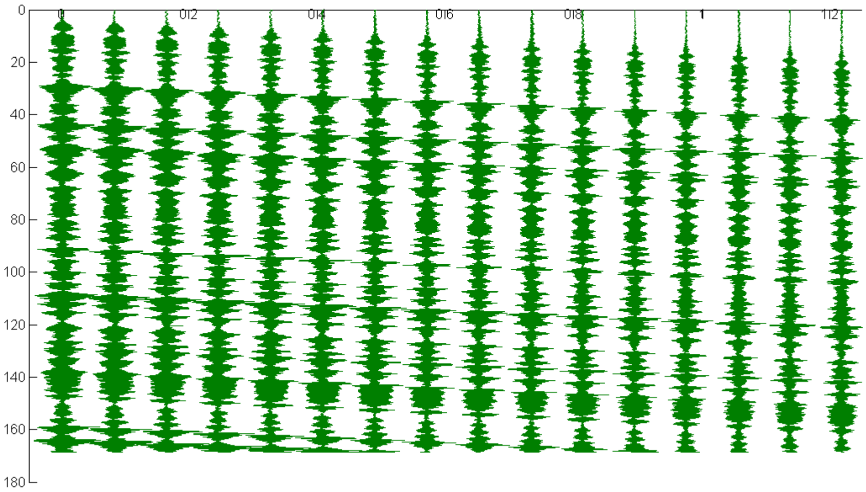

FIGURE 3.3: Probe measurement after cubic interpolation. The horizontal axis is $1.15\epsilon^2 k_p x$, the vertical axis is time in seconds. The surface elevation is normalized as $\frac{k_p}{5}\eta$.

In deterministic prediction of wave propagation, the quality of raw data is very important. Therefore missing data can significantly affect the prediction. A visual observation of serieses of plots of the measured time series confirmed that probe measurement nearest to the wave generator is the most affected by dropouts. A best strategy must be devised to get a representing time series that initialize the simulation. This subject will be discussed in Chapter 5 broadly.

3.2 Fourier Analysis

The surface elevation in equation 2.31 is going to be used in Chapter 4 to simulate the surface elevation at different probe positions. The first of the sixteen probe measurements is used to initialize deterministic prediction simulation of the wave propagation downstream of the wavemaker. A Fourier transform of this irregular timeseries is required to compute complex amplitudes of a regular wave components. Discrete Fourier transform (DFT) is applied to the time series by a Fast Fourier Transform (FFT) in Matlab.

For the probe positioned at $x = x_m$, consider a time series with length T discretized with a fixed time interval of Δt, then the data points are $t_n = n\Delta t$ where $n = 0, 1, 2, \ldots, N-1$ and N is the total number of data points. Omitting the viscous term, the discrete form of (2.31) is

$$\eta(x_m, t_n) = \sum_{j=0}^{N-1} Re\left[\hat{\eta}_j e^{-ik_j x_m + i\omega_j t_n}\right]. \tag{3.3}$$

T can be written in terms of the discrete time interval and the number of data points as

$$T = N\Delta t, \tag{3.4}$$

and the discrete frequency as

$$\omega_j = \frac{2\pi j}{T}, \tag{3.5}$$

where $j = 0, 1, 2 \ldots, N-1$.

For a spatial length L, discretized with a fixed spatial interval Δx, the data points are $x_m = m\Delta x$. Where $m = 0, 1, 2, \ldots, M-1$, M is the total number of data points in space and $L = M\Delta x$. In the linear model, the discrete wavenumber k_j can be computed from the dispersion relation (2.14) iteratively see Appendix B.2.

The complex amplitudes $\hat{\eta}_j$ are the discrete Fourier transform of the surface elevation (3.3) of the characteristic wave.

$$\hat{\eta}(\omega_j) = \frac{1}{N} \sum_{j=0}^{N-1} \eta(x = 0, t_n) e^{i\omega_j t_n}, \tag{3.6}$$

and the frequency spectrum will be

$$S(\omega_j) = |\hat{\eta}(\omega_j)|^2. \tag{3.7}$$

Chapter 4

Deterministic Prediction of Sea Waves using linear and weakly nonlinear models

It has been introduced that the simulation is initialized by the wave measurement at the first probe located nearest to the wavemaker. The simulated wave elevations at different probe locations are then compared with the respective measurements at each of the probe downstream of the wavemaker including the first one. Error criteria will be introduced to evaluate the accuracy of the models used and to find out the prediction region in space and time.

In Section 4.1, the linear wave model is implemented to simulate the propagation of long-crested wave, whereas in Section 4.2, the nonlinear wave model (NLS) is implemented to simulate the propagation.

.

4.1 Linear Model

4.1.1 Long-Crested Wave

4.1.1.1 Smoothing of time series

The sampling frequency $f = 200Hz$ and timestep $\Delta t = 1/f = 0.005s$ which is very small. The measured time series contains high frequency noise as shown in figure 4.1.

In the figure, the first ten seconds are shown from a single probe measurement.

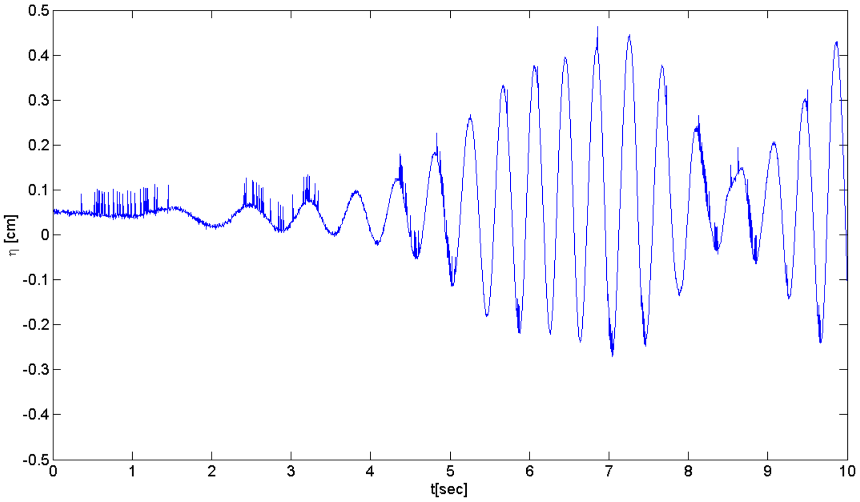

FIGURE 4.1: Typical time series with noise.

In this section, smoothing is done by removing the high frequency range in the frequency domain from the time series at all the probes. This is done without affecting the main signal. The steps are depicted in figure 4.2(a) to 4.2(c). A plot of the surface elevation before and after smoothing are shown in Appendix B.1.

The minimum frequency removed is $\omega(J = 2270) = 88.52s^{-1}$ compared to the peak frequency $\omega_p = \omega(j = 397) = 14.7272s^{-1}$ and the characteristic frequency $\omega_c = \omega(j \approx 392) = 14.5775s^{-1}$. The corresponding wavenumber $k(J = 2270) = 364.0915m^{-1}$ compared to the wavenumber corresponding to the peak frequency $k_p = k(j = 397) = 21.5127m^{-1}$ and the wavenumber corresponding to the characteristic frequency $k_c = k(j \approx 392) = 21.6621m^{-1}$, where $j = 0, 1, 2 \ldots, N - 1$ and $(J = j = 2270)$. The red lines in figure 4.2(b) are positioned at J. Hereafter we set $\omega(j) = 0$ for $J < j \leq N - J$.

4.1.1.2 Wave characterization

The work in this section is motivated by the paper (Trulsen[4]) and the symbols defined here are taken from there for the sake of agreement. The characteristic property of the time series at the first probe will be studied here. This is because, the simulation of the propagation of the wave at the rest of the probes is initialized by the time series measured at the first probe. The significant wave height and the characteristic amplitude can be estimated from the root-mean-square of the discrete time series as follows.

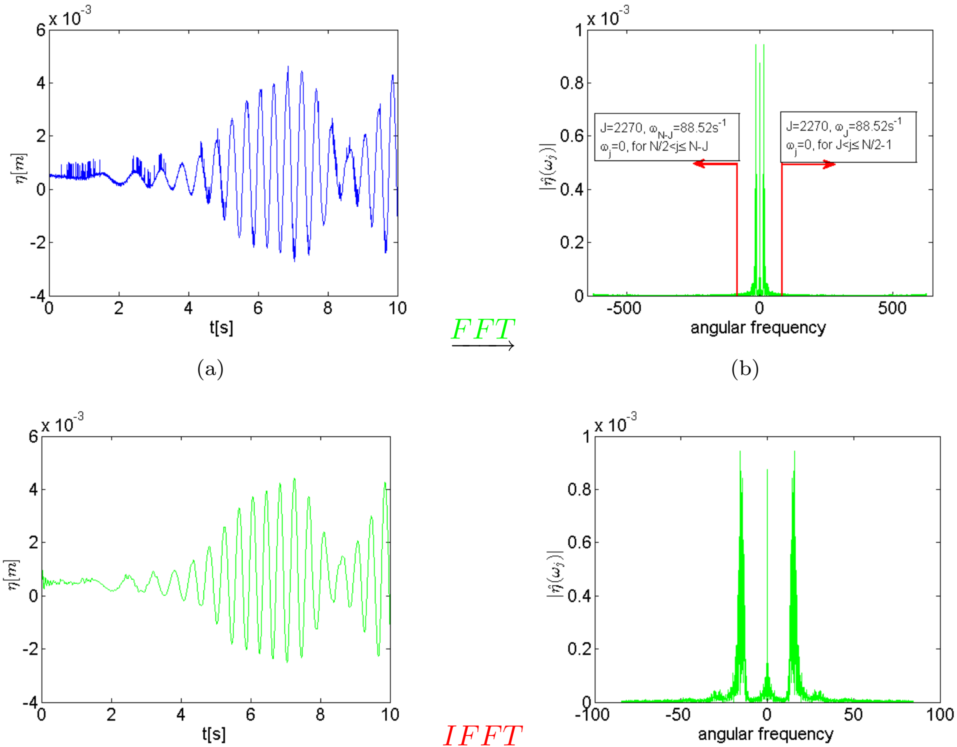

(a) (b)

(c) (d)

FIGURE 4.2: Smoothing:4.2(a) Time series with noise, 4.2(b) Fourier transform of 4.2(a) (contains frequency range which should be removed), 4.2(d) High frequency ranges are removed (contains frequency range which should be retained) and 4.2(c) Resulted from the inverse Fourier transform of 4.2(d) (smooth time series)

$$\begin{aligned} \sigma &= \sqrt{\frac{1}{N}\sum_{n=0}^{N-1}\eta_n^2} = 0.0033m. \\ H_s &= 4\sigma = 0.0132m. \\ a_c &= \sqrt{2}\sigma = 0.0047m. \end{aligned} \tag{4.1}$$

Where σ is the root mean square (quadratic mean) of the discrete time series, H_s and a_c are the significant wave height and the characteristic amplitude of the discrete time series (surface elevation) respectively.

The characteristic angular frequency of the discrete timeseries may be estimated by

$$\omega_c = \frac{\sum_j |\omega_j||\hat{\eta}_j|^2}{\sum_j |\hat{\eta}_j|^2} = 14.5272s^{-1}. \tag{4.2}$$

Where $\omega_j = \frac{2\pi j}{T}$ are angular frequencies and $\hat{\eta}_j$ the Fourier transform of the discrete time series given by equation 3.6. Note that the high frequency range is removed for

$j > J$ by smoothing as discussed in the preceding section. The summation range can be simplified by setting the limit as $j = 0, 1, 2, \ldots, J$ in (4.2) for only the right half of figure 4.3. The frequency spectrum given by equation 3.7 is depicted in figure 4.3.

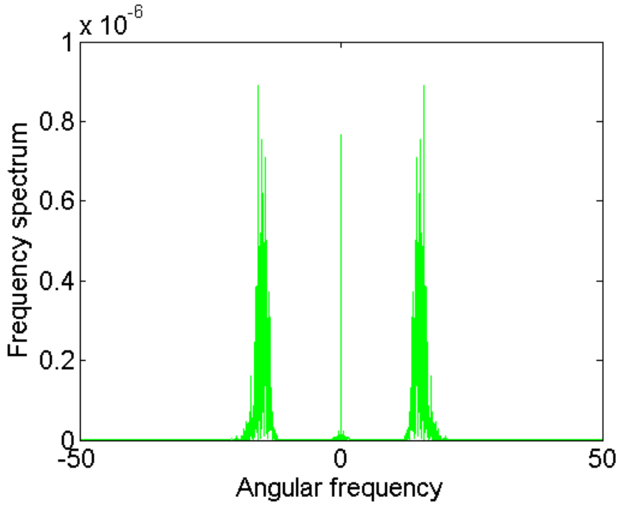

FIGURE 4.3: Frequency spectrum ($|\hat{\eta}(\omega_j)|^2$).

The corresponding characteristic frequency and period are estimated by $f_c = \frac{2\pi}{\omega_c}$ and $T_c = \frac{1}{f_c} = \frac{2\pi}{\omega_c}$. The characteristic wavenumber may be estimated by the infinite depth linear dispersion relation, $k_c = \frac{\omega_c^2}{g}$. The results are summarized in table 4.1.

TABLE 4.1: Characteristic and peak values of the discrete time series at probe 1 (in SI units)

Symbols	Values	Description	Symbols	*Values*	Description
ω_p	14.5272	peak ang. frequency	ω_L	12.0	lowest frequency
ω_c	14.5775	*Characteristic ang. frequency*	ω_H	18.5	highest frequency
k_p	21.5127	*wavenumber correspond to* ω_p	c_L	0.8182	fastest ph[a]. speed
k_c	21.6621	*wavenumber correspond to* ω_c	c_H	0.5327	slowest ph. speed
T_p	0.4325	*wave period correspond to* ω_p	c_{gP}	0.3406	c_{gP}[b].
T_c	0.4310	*wave period correspond to* ω_c	c_{gL}	0.4104	fastest g[c]. velocity
a_p	0.0027	peak amplitude	c_{gH}	0.2712	*slowest g. velocity*
a_c/H_s	0.0047/ 0.0132	characteristic amp./s.w.h[d].	$\epsilon = k_c a_c$	0.1045	charac. steepness

---

[a] phase.
[b] group velocity corresponding to ω_p.
[c] group.
[d] significant wave height.

It is useful to determine the peak, lowest and highest velocity components of the wave. The results can be compared with the characteristic values discussed before. The components are mainly useful to study the norm of the error in connection with the prediction region.

To find the frequency components present in the measured surface elevation, it is possible to start from the Fourier transform of the full length time series. However it will be effective and gives more sense to select a time window which represent an input time trace of the characteristic wave which initiates the prediction. Let us consider a time trace of length 20s, t ∈ [40, 60]s for the first realization. For single realization, the plot of the spectrum of the input time trace looks like the one shown in figure 4.3, which is difficult to pick the frequency components. Thus it is necessary to take many realizations of such traces and take the average so that the spectrum becomes smooth. Ensemble averaging has been used to smooth the spectrum appropriately. The time interval for the first, second and j^{th} realizations are $t_{40:60}$, $t_{40+\Delta t:60+\Delta t}$, $\dots$,$t_{40+(j-1)\Delta t:60+(j-1)\Delta t}$. The frequency spectrum for j^{th} realization is then $S_j = |\hat{\eta}_j|^2$. For M numbers of realization, the average value will be

$$S_{averaged} = \frac{1}{M}\sum_{j=1}^{M} S_j. \tag{4.3}$$

A plot of equation 4.3 is shown in figure 4.4 for 15000 realizations. In the figure, the lowest and highest frequency components are also shown by arrows. The frequencies and the corresponding phase speed and group velocity components are summarized in table 4.1.

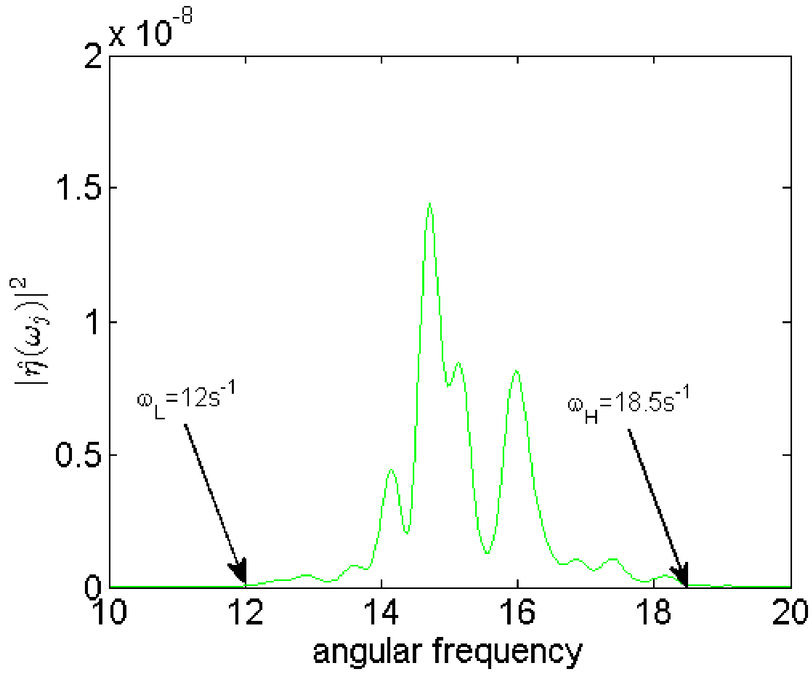

Figure 4.4: Frequency spectrum with frequency components shown.

4.1.1.3 Forecast by linear model.

A plot of subsequently measured time series are shown in figure 4.5. In the figure the time windows correspond to those shown in figure 5.3 left plot, i.e. the slopes of the slanted lines are group velocities c_{gP} c_{gL} and c_{gH}. Where c_{gP} is group velocity which correspond to the top of the spectrum, c_{gL} is the fastest group velocity which correspond to the lowest frequency component (ω_L) located to the left of the peak spectrum and c_{gH} is the slowest group velocity which correspond to the highest frequency component (ω_H) located to the right of the peak spectrum. At any location to the left of the line with slope c_{gH} the slowest group of the input trace have not arrived and at any location to the right of the line with slope c_{gL} the fastest group of the input trace have already passed.

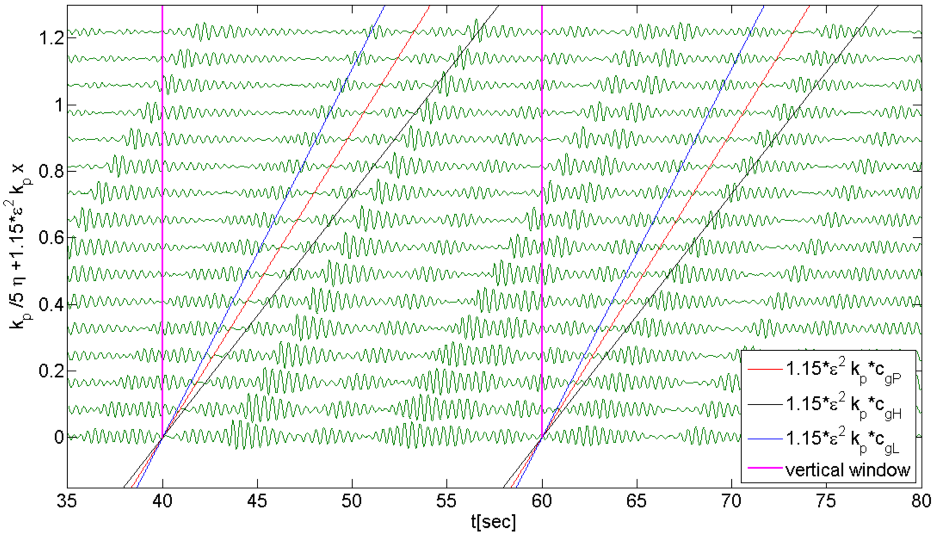

FIGURE 4.5: Measured time series with different types of windows.

In the following, the main steps concerning the prediction of the surface elevation in space and time will be summarized sequentially.

- Measure the wave elevation in time at different probe locations. This step is not part of the thesis. The possible schematic diagram of the experimental arrangement as well as the plots of available experimental data are depicted in Chapter 3.

- Prepare the measured data for the next step. Time series measurement at each probe is filtered and the characteristics of the time series measured at the first probe is studied in the preceding section.

- The Fourier transform of the time series measurement at the first probe is computed to get the complex amplitudes ($A_j = \hat{\eta}(\omega_j)$). The complex amplitude A_j contains both the real amplitudes and phases. FFT algorithm has been used in Matlab to find the discrete Fourier transform.

$$\hat{\eta}(\omega_j) = \frac{1}{N}\sum_{N=0}^{N-1} \eta_n e^{i\omega_j t_n}. \tag{4.4}$$

- The discrete angular frequencies are know in frequency domain, see Chapter 3 for details. Once we know $\omega_j = \frac{2\pi j}{T}$, we can calculate the wavenumber from the dispersion relation $k_j = \frac{\omega_j^2}{(g+\frac{\sigma k_j^2}{\rho})\tanh(k_j h)}$ iteratively for every j discrete points (see Appendix B.2), where $j = 1, 2, 3 \dots 2270$ and for $2270 < j < \frac{N}{2} - 1$, ω_j is set to equal null to smooth the surface elevation (discussed in Section 4.1.1.1).

- Using the parameters defined above and the theories in Chapter 2 and 3, the spatiotemporal model that forecast the real time wave propagation will be constructed.

  $$\eta(x,t) = Re(\sum_j e^{(-2\nu k_j^2 x/c_g)} A_j \exp -i(k_j x - \omega_j t)). \tag{4.5}$$

  Where ν is the coefficient of kinematic viscosity and c_g is the group velocity.

- The forecasted surface elevation by equation 4.5 is shown in figure 4.6. One can compare the forcasted surface elvation with the experimental surface elevation shown in figure 4.5.

Figure 4.6 shows the forecasted surface elevation at all the probes. In the figure various time windows are also depicted.The lines, representing the windows, correspond to those shown in figure 5.3 left diagram.

A comparison of measured and simulated time series at the first four probes is depicted in figure 4.7 for the others see Appendix B.3. The plots are within a moving time window that moves with group velocity corresponding to the peak spectrum shown in figure 4.4. As can be seen from the figures the error is null at the first probe and increases with distance.

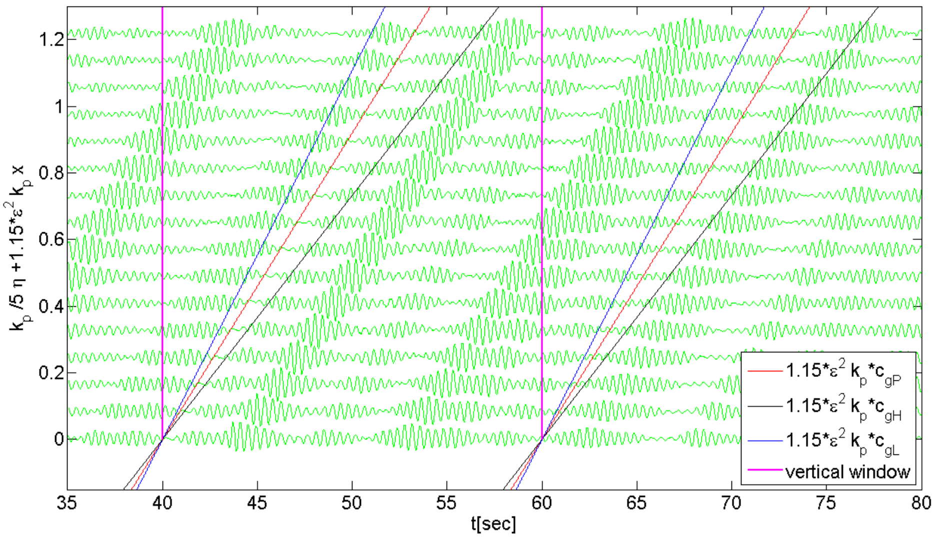

FIGURE 4.6: Simulated time series with different types of windows.

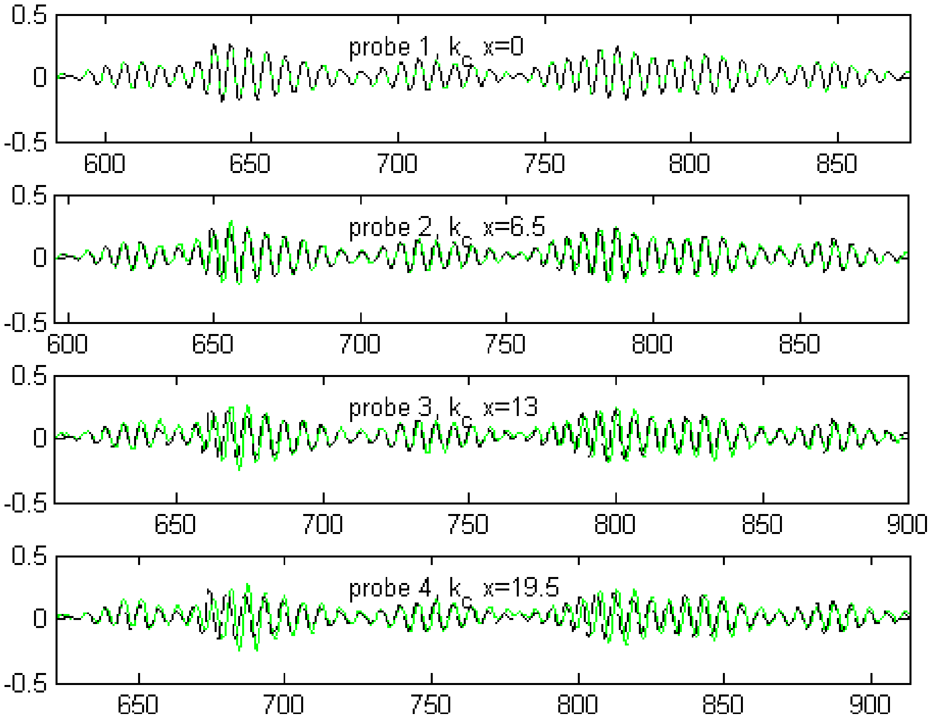

FIGURE 4.7: Measured and simulated (green solid curves) time series at probes 1, 2, 3 and 4, the figures are within a moving time window with velocity c_{gP}.

4.1.1.4 Prediction error

Prediction error in space.

Now, it is time to calculate the sum of error at each of the probe. The error calculation is done within a moving time window which moves with various group velocity components contained in the input trace.

Normalized error is then computed by

$$e(x) = \frac{\sum_i (\eta_b(x,t_i) - \eta_m(x,t_i))^2}{\sum_i (\eta_b(x,t_i)^2 + \eta_m(x,t_i)^2)}, \tag{4.6}$$

where $\eta_b(x,t_i)$ is simulated surface elevation and $\eta_m(x,t_i)$ is experimentally measured surface elevation. The types of windows used are:

1. Group velocity which correspond to the top of the spectrum → c_{gP},
2. The slowest group velocity → c_{gH},
3. The fastest group velocity → c_{gL},
4. And a vertical window formed by two vertical lines at $t = 40s$ and $t = 60s$.

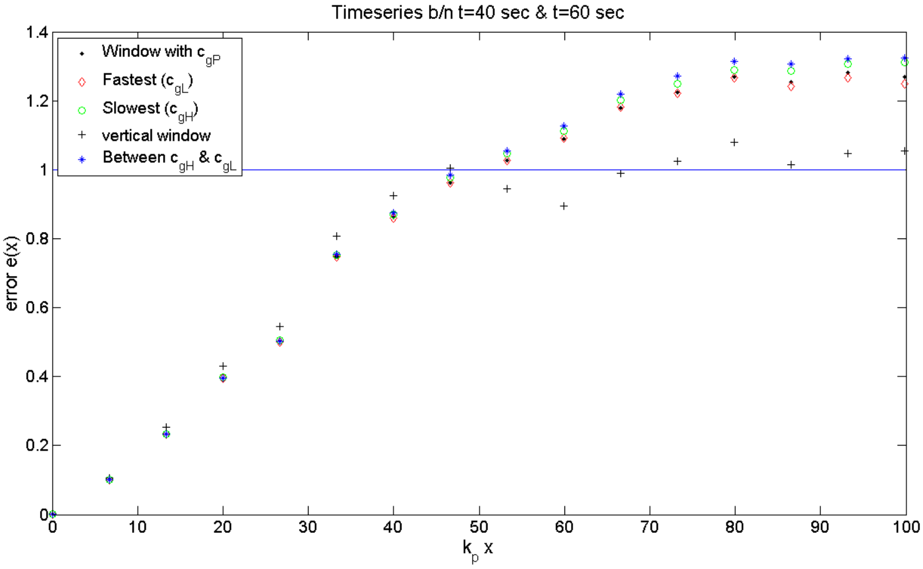

FIGURE 4.8: Normalized error as a function of normalized distance. Initialized by the time series at $x = 0$ for $t \in [40, 60]s$.

Graphs of equation 4.6 are shown in figure 4.8 and 4.9: The graphs in figure 4.8 are initialized by part of the time series at the first probe. For $e(x) \leq 1$ and $k_p x \in [0, 50)$, the error calculated within the vertical window is the largest of the others. Where as the error within the window formed by lines with slopes equal to c_{gP} and c_{gL} are almost equal and are the least of the others. The error graphs in figure 4.9 are initialized by the whole time series of the first probe. For $e(x) \leq 0.6$ the error within the various windows are almost equal. Whereas for $0.6 < e(x) \leq 1$ and $k_p x \leq 50$, the error within the vertical window and the window formed by the lines with slope c_{gH} and c_{gL} are the largest of the others but the difference is not significant. Particularly, the error within the vertical window becomes unstable for $k_p x > 50$. Since the error calculation is initialized by the whole time series at $x = 0$, the resulting error within the vertical window is comparable with the others for $k_p x \in [0, 50)$. In figure 4.9, the error within the vertical window is significantly less for $k_p x > 51$, this is due to the wave component containing the significant part of the error has gone out from the vertical window (waves above the line **B** in figure B.11), while wave component containing insignificant part of the error has entered the vertical window (waves above the line **A** in figure B.11).

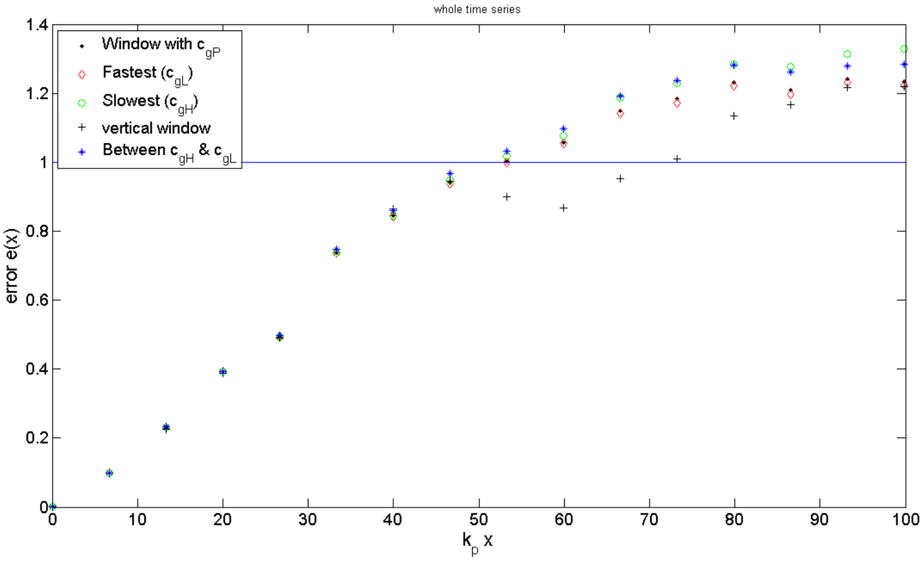

FIGURE 4.9: Normalized error as a function of normalized distance. Initialized by the whole time series at $x = 0$.

Space-time prediction error (error contor).

In this section part of the time series at the first probe is used to initiate the simulation of wave propagation along the wave tank and then to calculate the surface prediction error. For one realization the simulation looks like the one shown in figure 4.10 (zoomed to show the surface elevation at the first seven probes). Based upon such a simulation, the space-time prediction error can be calculated with equation 4.7.

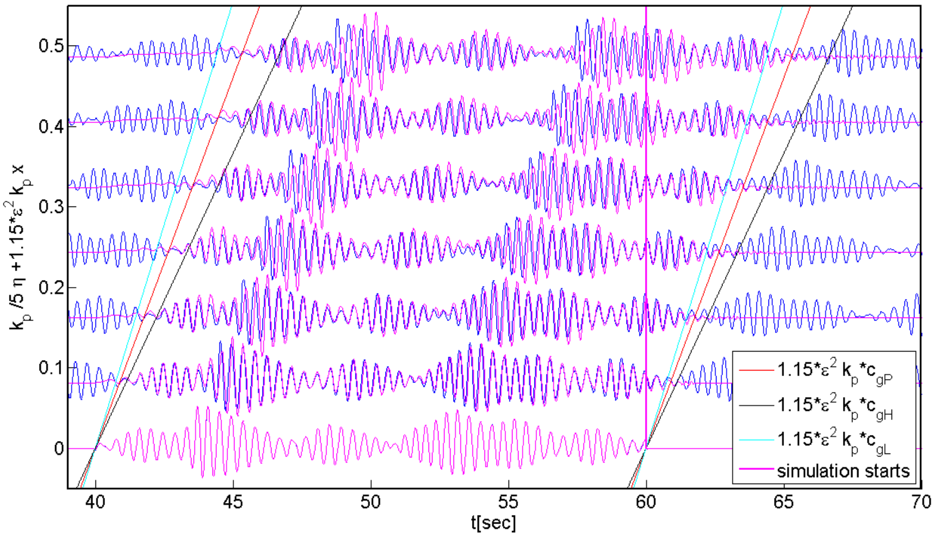

FIGURE 4.10: Measured and simulated time series for one realization for probes one through seven.

$$E(t,x) = \frac{(\eta^b(t,x) - \eta^m(t,x))^2}{(\eta^b(t,x))^2 + (\eta^m(t,x))^2}, \tag{4.7}$$

where $E(t,x)$ is space-time prediction error, $\eta^m(t,x)$ is experimentally measured surface elevation and $\eta^b(t,x)$ is simulated surface elevation.

A contor plot of $E(t,x)$ for one realization is not clearly visible. Therefore it necessary to take many such realizations and average them together to get good resolution of the contor plot. Ensemble averaging is used to average the realizations and the steps are summarized below.

Consider $\eta^m(t_n, x_i)$ is measured surface elevation, where $n = 0, 1, 2, \ldots, N-1, \quad N = 33736$ is total number of data points and $i = 1, 2, \ldots, 16$ are probe locations.

- Initialization of j^{th} realization.

  $\eta^m_j(t_{0:8000+j-1,x_1}) = 0,$

  $\eta^m_j(t_{8000+j:12000+j-1,x_1}) = \eta^m(t_{8000+j:12000+j-1,x_1}),$

  $\eta^m_j(t_{12000+j-1:N,x_1}) = 0.$

  Figure 4.10 shows measured and simulated surface elevation at probe x_i for realization $j = 1$. m stands for measured, t_{8000} correspond to $t = 40s$ and t_{12000} correspond to $t = 60s$.

- Surface elevation simulation initialized by j^{th} realization

For every j^{th} realization, simulate surface elevation η_j^b at x_i (prediction (probe) location) using equation 4.5. b stands for simulated.

- Space-time error calculation for j^{th} realization.

$$E_j(t,x) = \frac{(\eta_j^b(t,x) - \eta_j^m(t,x))^2}{(\eta_j^b(t,x))^2 + (\eta_j^m(t,x))^2}. \tag{4.8}$$

- Calculate the average error ($E_{average}(t,x)$).

  Equation 4.8 finds the error for j^{th} realization. Let M be numbers of realization, then the average error becomes

$$E_{average}(t,x) = \frac{1}{M}\sum_{m=0}^{M} E_j(t,x) \tag{4.9}$$

- Implementing in Matlab.

  Results from each realization of the error function (4.8) are first arranged to average with all the other error functions of the rest of the realizations. Every j^{th} realization moves j step forward. To compensate the forward movement and average them together, the error function for each realization should move $j-1$ step backward as in (4.10)

$$E(t_{8001:18000,x_i}) = E_j(t_{8000+j:18000+j}, x_i) \tag{4.10}$$

  Finally (4.9) is used to average the results from each realizations together.

The contor plot in figure 4.11 shows the space-time prediction error for two different realizations. The upper two are results of 200 realizations and the lower two contor plots are resulted from 2000 realizations. In each of the contor plot, two bounding slanted lines are depicted. The lines have a slope equal to the group velocity corresponding to the peak spectrum.

4.2 Nonlinear Model

In this section, the nonlinear models summarized in Section 2.2 will be validated. The section covers only the cubic Schrödinger equation for long-crested waves. The modified nonlinear Schrödinger (MNLS) equation for long-crested waves and the nonlinear models for short-crested waves are not part of the thesis. The reconstruction of the wave elevation is done as presented in Section 2.2 i.e. the weakly nonlinear surface is

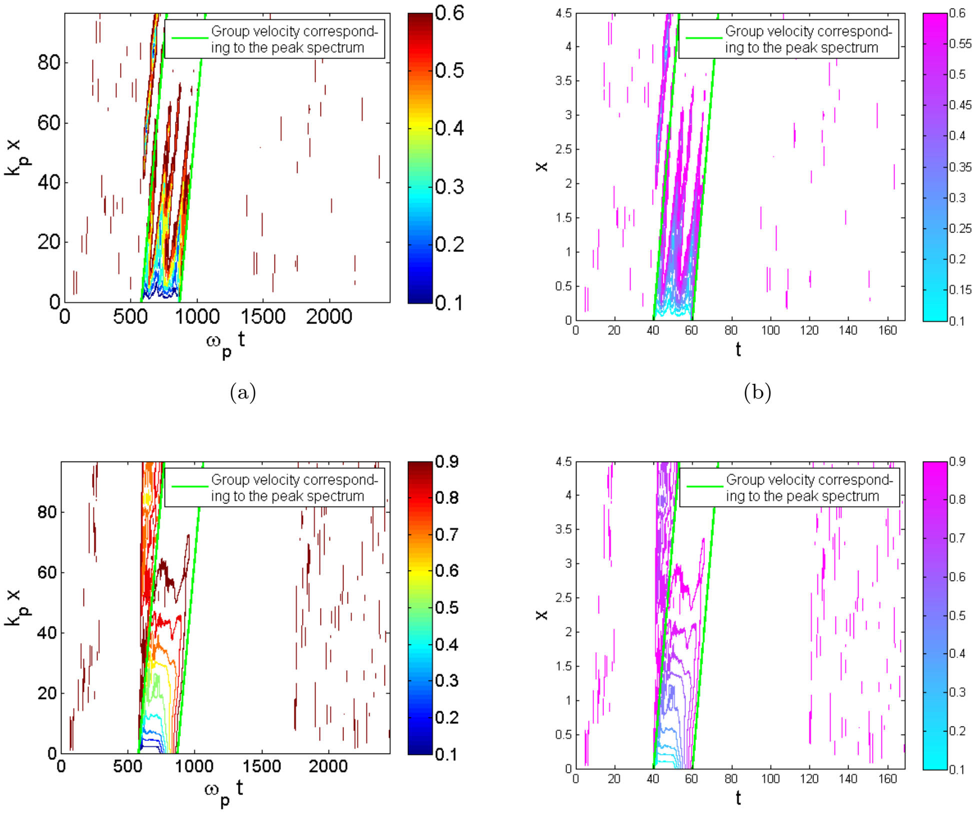

(a) (b)

(c) (d)

FIGURE 4.11: Space-time error contor together with lines which have a slope equal to the group velocity corresponding to the peak spectrum:4.11(a) Normalized contor plot for 200 realizations, 4.11(b) Contor plot for 200 realizations (not normalized), 4.11(c) Normalized contor plot for 2000 realizations 4.11(d) Contor plot for 2000 realizations (not normalized).

the superposition of free and nonlinearly forced waves. Smoothing the time series and characterization of the wave discussed in Sections 4.1.1.1 and 4.1.1.2 are valid in this section.

$$\phi = \bar{\phi} + Re\left(Ae^{-i(k_c x-\omega_c t)} + A_2 e^{-2i(k_c x-\omega_c t)} + A_3 e^{-3i(k_c x-\omega_c t)} + \dots\right), \tag{4.11}$$

$$\eta = \bar{\eta} + Re\left(Be^{-i(k_c x-\omega_c t)} + B_2 e^{-2i(k_c x-\omega_c t)} + B_3 e^{-3i(k_c x-\omega_c t)} + \dots\right), \tag{4.12}$$

where $B(\mathbf{r},t)$, $B_2(\mathbf{r},t)$ and $B_3(\mathbf{r},t)$ are the first, second and third harmonic complex amplitudes of the surface elevation respectively while $A(\mathbf{r},t)$, $A_2(\mathbf{r},t)$ and $A_3(\mathbf{r},t)$ are the corresponding complex amplitudes of the velocity potential. $\bar{\eta}(\mathbf{r},t)$ is the zeroth harmonic of surface elevation with slow drift velocity $\bar{\phi}(\mathbf{r},t)$. Here $\mathbf{r} = (x,y)$ is a horizontal position vector.

4.2.1 Long-Crested Wave

4.2.1.1 Initialization

In this section we are going to implement numerical methods to solve the nonlinear equation. The methods employed here require Fourier analysis

Let us denote $B(x, \mathcal{T}_j)$ by B_j. Then the discrete Fourier transform of B_j is

$$\hat{B}_n = F[B_j] = \frac{1}{N} \sum_{j=0}^{N-1} B_n e^{-in\mathcal{T}_j}, \quad -\frac{N}{2} \leq n \leq \frac{N}{2} - 1, \tag{4.13}$$

and the inverse Fourier transform gives B_n as

$$B_j = F^{-1}[\hat{B}_n] = \sum_{n=-N/2}^{N/2-1} \hat{B}_n e^{in\mathcal{T}_j}, \quad j = 0, 1, \ldots, N-1, \tag{4.14}$$

where F and F^{-1} are the discrete Fourier transform and its inverse respectively. For now $\mathcal{T}_j$ is temporal grid point.

The measured time series at $x = 0$ is used to initialize the simulation. The characteristic properties of the waves at this location are computed and the parameters are detailed in Section 4.1.1.2. To approximate B, let us first write the harmonic expansion (2.37) for a given characteristic wave properties as in (4.15), the same way as in Trulsen. [19] with opposite sign in the exponents.

$$\begin{aligned} B = 2(\eta - \bar{\eta})e^{i(k_c x - \omega_c t)} - B^* e^{2i(k_c x - \omega_c t)} - B_2 e^{-i(k_c x - \omega_c t)} \\ -B_2^* e^{3i(k_c x - \omega_c t)} - B_3 e^{-2i(k_c x - \omega_c t)} - B_3^* e^{4i(k_c x - \omega_c t)} - \ldots \end{aligned} \tag{4.15}$$

Then B is calculated by first taking the Fourier transform of the first term on the right side of equation 4.15. Actually B can be computed from the Fourier transform of $2\eta e^{-i(\omega_c t)}$. The Fourier transformed function is then bandpass filtered around the characteristic angular frequency $[0, 2\omega_c]$ see [5]. Plots of the square of the first term on the right side of equation 4.15, the bandpass filtered around ω_c, the first harmonic complex amplitude and the second harmonic complex amplitude of the cubic Schrödinger are shown in figure 4.12. A part of measured surface elevation at $x = 0$ and its envelope are depicted in figure 4.13.

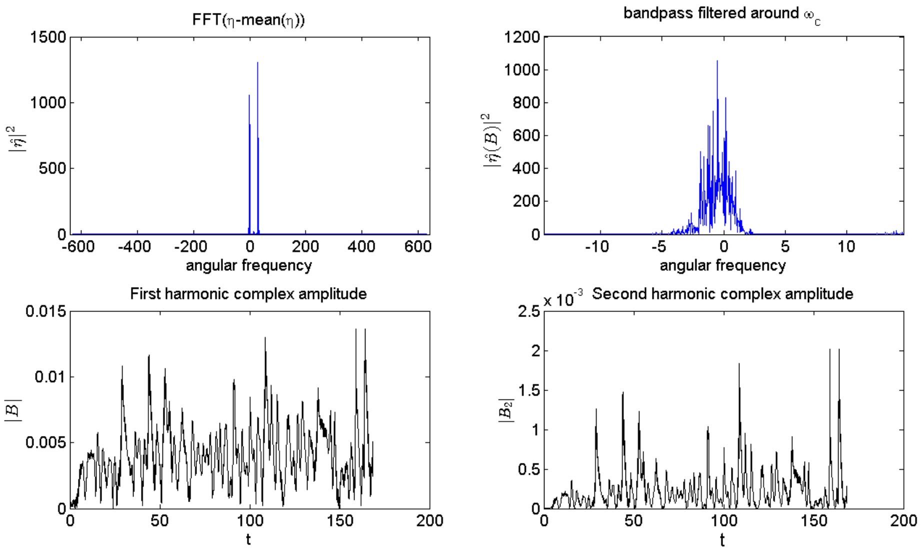

FIGURE 4.12: Upper left: Frequency spectrum, Upper right: Frequency spectrum after bandpass filtered around ω_c, Lower left: First harmonic complex amplitude (B), Lower right: Second harmonic complex amplitude (B_2).

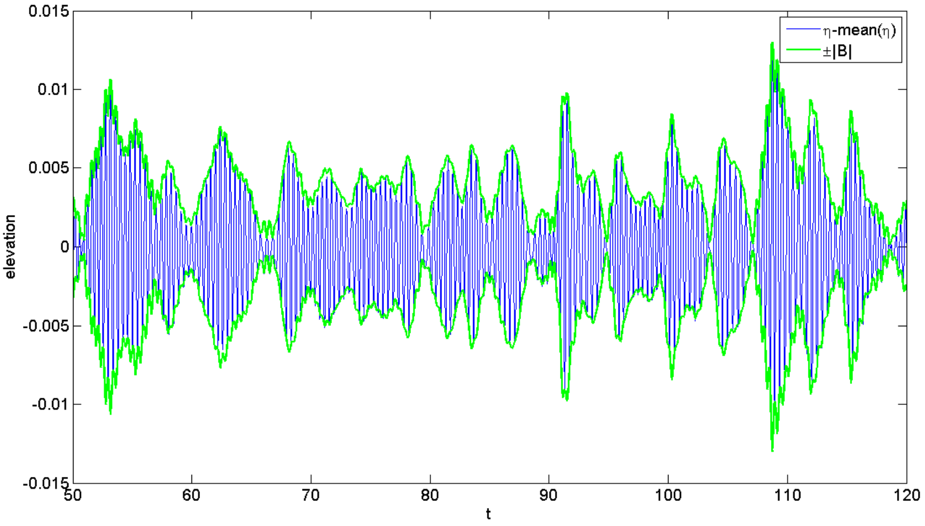

FIGURE 4.13: Surface elevation at $x = 0$ and its envelope.

4.2.1.2 Forcast by third order nonlinear Schrödinger equation (NLS)

The spatial evolution of third order nonlinear Schrödinger equation for long crested waves has already been introduced in equation 2.39 for infinitely deep water. For convenience let us write the equation again here.

$$\frac{\partial B^*}{\partial x^*} + \frac{2k_c}{\omega_c}\frac{\partial B^*}{\partial t^*} + \frac{ik_c}{\omega_c}\frac{\partial^2 B^*}{\partial t^{*2}} + ik_c^2|B^*|^2 B^* = 0. \tag{4.16}$$

In (4.16), $*$ stands for variables with dimension. Assume $\frac{|\Delta k|}{k_c} = O(\epsilon)$, $(k_c H)^{-1} = O(\epsilon)$. The space evolution of a temporal cubic nonlinear Schrödinger (NLS) (4.16) is normalized with nondimensional variables $t = \omega_c t^*$, $x = k_c x^*$ and $B = k_c B^*$ and presented in dimensionless form as

$$\frac{\partial B}{\partial x} + 2\frac{\partial B}{\partial t} + i\frac{\partial^2 B}{\partial t^2} + i|B|^2 B = 0. \tag{4.17}$$

Equation 4.17, can be solved by different methods which are introduced below, of these methods the split-step Fourier has been used in this thesis.

Lo and Mei [23] have employed split-step pseudo-spectral method to solve the boundary value problem of the modified nonlinear Schrödinger equation (MNLS). In this article the linear and nonlinear terms are summed at each spatial step as

$$\frac{\partial B}{\partial x} = L(B) + N(B), \tag{4.18}$$

where $L(B)$ and $N(B)$ are the linear and the nonlinear terms involved in the equation. At each spatial step the linear and nonlinear equations are solved independently such that the current solution is used as an initial condition to the next spatial step. First the nonlinear part is solved in space with a midpoint finite-difference approximation. Then the solution from nonlinear term is applied to the linear terms to get the complex amplitudes in space

$$B(x + \Delta x) = F^{-1}\left(e^{iP\Delta x} F\left(\tilde{B}(x + \Delta x)\right)\right), \tag{4.19}$$

where F and F^{-1} are the discrete Fourier transform and inverse discrete Fourier transforms, the parameter P is constant as we shall see soon and $\tilde{B}(x + \Delta x)$ is the solution from the nonlinear term approximated by finite-difference method, see the whole derivation for NLS in Appendix C.1. A slight modification has also been proposed by Zhang and Li.[24] that does not require a periodic boundary condition. The methods discussed so far are not used in this paper. In the following we will discuss the method used in this thesis.

Taha and Ablowitz [25] have employed various methods to solve the temporal evolution of nonlinear Schrödinger equation numerically, two of the methods used are split step and pseudospectral methods. Here a brief summary of the split step Fourier method will be presented for a spatial evolution of NLS equation 4.17. Let us write the evolution equation by first multiplying both sides of (4.17) by imaginary number i.

$$i\frac{\partial B}{\partial x} = (\mathcal{L} + \mathcal{N})\, B, \tag{4.20}$$

where $\mathcal{L}$ and $\mathcal{N}$ are linear and nonlinear operators respectively

$$\mathcal{L} = \left(-2i\frac{\partial}{\partial t} + \frac{\partial^2}{\partial t^2}\right), \qquad \mathcal{N} = |B|^2. \tag{4.21}$$

The split step Fourier method has an approximate solution with in a discrete propagating length Δx. As mentioned before the linear (dispersive) and nonlinear effects act independently. In simulating the spatial evolution from x to $x + \Delta x$, the first step is to consider the nonlinear term alone setting $\mathcal{L} = 0$ in equation 4.20 then the next step is to consider the linear terms alone setting $\mathcal{N} = 0$. Mathematically

$$B(x + \Delta x, t) \approx e^{-i\Delta x\mathcal{L}} e^{-i\Delta x\mathcal{N}} B(x, t), \tag{4.22}$$

subjected to a boundary condition $B(0, t)$. The error from using such an approximate solution can be estimated by comparing it with the exact solution of (4.20). Which is

$$B(x + \Delta x, t) = e^{-i\Delta x(\mathcal{L}+\mathcal{N})} B(x, t). \tag{4.23}$$

For noncommuting operators, Baker-Hausdroff formula [26] leads to a conclusion that the split step Fourier method is accurate to $O(\Delta x^2)$, (see Agrawal [27]). The accuracy can be estimated as follows.

The Baker-Hausdorff formula for two noncommuting operators $\hat{a}$ and $\hat{b}$,

$$exp\,(\hat{a})\, exp\left(\hat{b}\right) = exp\left(\hat{a} + \hat{b} + \frac{1}{2}\left[\hat{a}, \hat{b}\right] + \frac{1}{12}\left[\hat{a} - \hat{b}, \left[\hat{a}, \hat{b}\right]\right] + \dots\right), \tag{4.24}$$

where $[\hat{a}, \hat{b}] = \hat{a}\hat{b} - \hat{b}\hat{a}$. This shows that, the noncommutating nature of the operators $\mathcal{L}$ and $\mathcal{N}$ is ignored by the split-step Fourier method. Replacing the operators $\hat{a}$ and $\hat{b}$ in (4.24) by $\Delta x\mathcal{L}$ and $\Delta x\mathcal{N}$ respectively, the dominant error is found to be from the commutator $\frac{1}{2}\Delta x^2[\mathcal{L}, \mathcal{N}]$. Thus, the split-step Fourier method is accurate to $O(\Delta x^2)$. If the operators $\mathcal{L}$ and $\mathcal{N}$ were assumed to commute with their commutator, the result would have been

$$e^{-i\Delta x\mathcal{L}}e^{-i\Delta x\mathcal{N}}B(x,t) = e^{-i\Delta x(\mathcal{L}+\mathcal{N})-\frac{1}{2}\Delta x^2[\mathcal{L},\mathcal{N}]}B(x,t). \tag{4.25}$$

For the temporal descretization, using numerical method involves truncation of the infinite interval to a finite interval $[a,b]$. This implies that the constants a and b chosen in such a way that the boundaries do not affect the propagation of the wave. So we shall perform the simulation in a periodic domain of 2π such that $B(x,a) = B(x,b)$ for $x \in [0,L]$. Thus the boundary conditions for NLS will be

$$B(x,0) = B(x,2\pi). \tag{4.26}$$

The normalization to $[0,2\pi]$ is done using the transformation formula $\mathcal{T} = 2\pi(t-a)/(b-a)$. For convenience let us write (4.17) in normalized form

$$i\frac{\partial B}{\partial x} = -i2p_1\frac{\partial B}{\partial t} + p_2\frac{\partial^2 B}{\partial t^2} + |B|^2B, \tag{4.27}$$

where $p_1 = \frac{2\pi}{T}$ and $p_2 = \left(\frac{2\pi}{T}\right)^2$.

The interval $[0,2\pi]$ discretized by N equal points, with spacing $\Delta\mathcal{T} = 2\pi/N$. $B(x,\mathcal{T}_j)$ is numerically defined only on the temporal grids points $\mathcal{T}_j = 2\pi j/N$, $j = 0,1,\ldots,N$. See [23, 25, 28] for more detail.

In (4.22), the exponential operator $e^{-i\Delta x\mathcal{L}}$ can be evaluated in Fourier domain. If we apply Fourier transform to both sides of (4.22)

$$F[B(x+\Delta x,\mathcal{T}_j)] = F[e^{-i\Delta x\mathcal{L}}e^{-i\Delta x\mathcal{N}}B(x,\mathcal{T}_j)]. \tag{4.28}$$

The temporal derivatives of B in the linear subproblem can be computed in Fourier domain. In Fourier domain the first order temporal derivative is $F^{-1}[e^{inp_1}F[B_j]]$, and the second order temporal derivative is $F_j^{-1}[e^{-n^2p_2}F_n[B_j]]$. See Appendix C.1 for such representation. The solution at each spatial step is then

$$B(x+\Delta x,\mathcal{T}_j) = F^{-1}[e^{-i\Delta x\left\{(in)(2p_1)+((in)^2p_2)\right\}}F[e^{-i\Delta x\mathcal{N}}B(x,\mathcal{T}_j)]]. \tag{4.29}$$

After multiplication and substitution of constants and the operator $\mathcal{N}$, the final result becomes

$$B(x+\Delta x,\mathcal{T}_j)=F^{-1}[e^{-i\Delta x\{\frac{4\pi n}{T}-(\frac{2\pi n}{T})^2\}}F[e^{-i\Delta x|B(x,\mathcal{T}_j)|^2}B(x,\mathcal{T}_j)]]. \tag{4.30}$$

The method is second order accurate in Δx and all order in Δt. Once we get the first harmonic complex amplitudes (4.30) at all the probes, the reconstruction of the surface elevation will be achieved by using second order reconstruction (2.40) . The reconstructed surface elevation in dimensionless form is then

$$\eta = Re\left(Be^{-i(x-t)}+B_2e^{-2i(x-t)}\right). \tag{4.31}$$

Equation 4.31 has been employed to simulate the surface elevation at different probe locations along the wave tank. Figure 4.14 depicts a zoomed part of the wave elevation simulated using NLS equation (4.31). The simulation is initialized by the measured timeseries at $x = 0$.

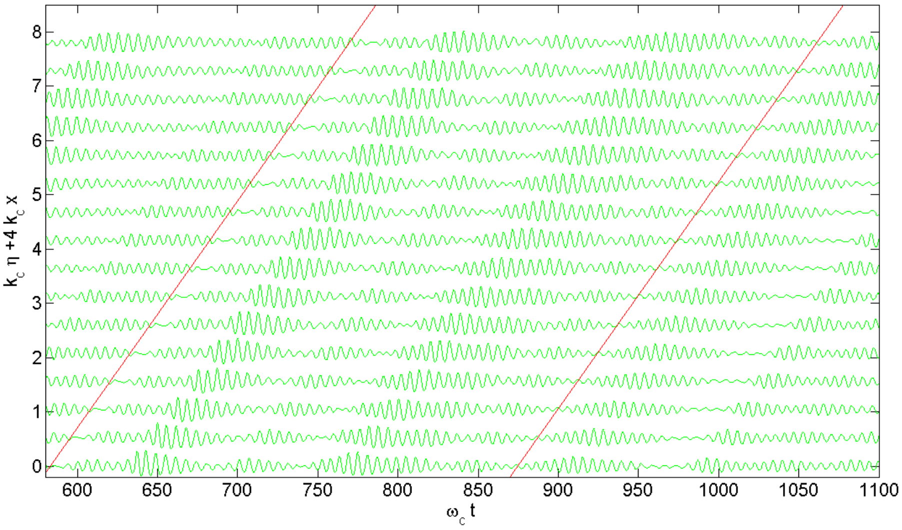

FIGURE 4.14: Predicted surface elevation by NLS equation.

Experimentally measured together with NLS simulated (predicted) surface elevation for the first four probe positions are shown in figure 4.15 for the others see figure-B.4 and B.5 in Appendix B.4. It has been observed that, measured time series and the first harmonic complex amplitude B at $x = 0$ are not in harmony close to $t = 0$. This has caused the NLS simulated surface elevation to not fit properly with the experimentally measured surface elevation. The effect may extend to result in a larger NLS prediction error.

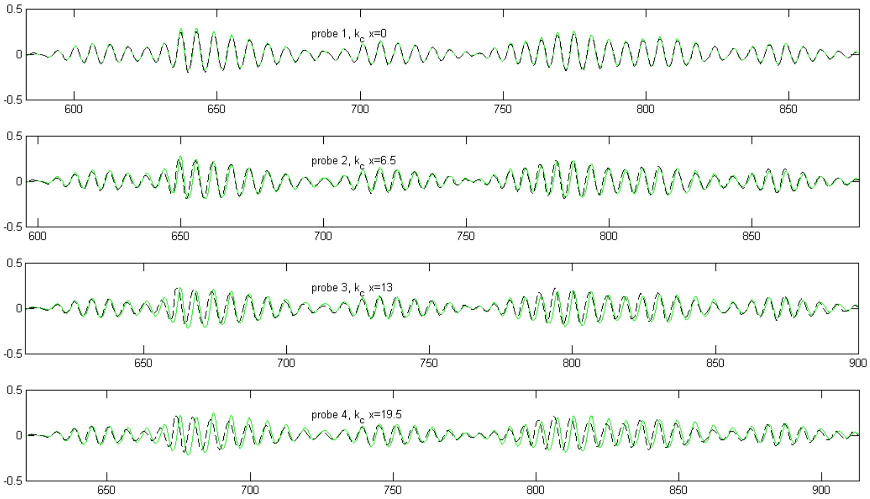

Figure 4.15: Measured (dashed curves) and NLS predicted (green solid curves) surface elevation for probes 1 to 4.

4.2.1.3 Prediction error resulted from NLS equation simulation

The methods employed to calculate the normalized error within a moving time window and the space-time prediction error for the linear model case were discussed in Section 4.1.1.4. As far as the error calculation is concerned the methods used in the linear model will still apply here too. The only difference here is that NLS equation is used to carry out the prediction in space.

Prediction error in space

The normalized error $e(x)$ of linear and NLS simulations, calculated within a moving time window are shown in figure 4.16. The linear simulation is better than NLS simulation prediction error.

In fact a better result was expected from NLS simulation as per the references [4, 19]. One reason to such discrepancy is that using different data may result in different normalized error. The second possible reason is that the simulated and measured surface elevations were not properly fitted. Another simulation is carried out in behalf of the first reason, with the simulation initialized by the time series at $x = 0$ for t $\in [8, 28]s$. The resulting graphs are now reversed, see figure B.6 in Appendix B.4. NLS simulation is now better than linear simulation prediction error.

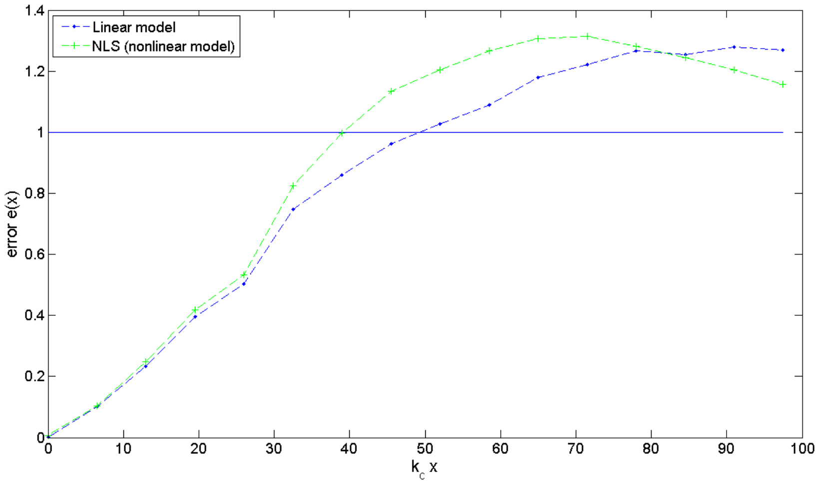

FIGURE 4.16: Normalized error for linear and NLS simulation. The simulation is initialized by time series at $x = 0$ for t $\in [40, 60]s$

Space-time prediction error (error contor). A space-time prediction error $E(t, x)$ calculation for each realization is carried out using equation 4.7 as before , $\eta^m(t, x)$ is experimentally measured surface elevation and $\eta^b(t, x)$ is now NLS simulated surface elevation. All the steps used in space-time prediction error in Section 4.1.1.4 are still valid. The only difference here is that $\eta^b(t, x)$ is simulated by NLS equation (4.31). Results from each realizations are averaged employing equation 4.9 to get the desired contor plot. Here the first realization is initialized by time series at $x = 0$ for t $\in [8, 28]s$ for better resolution.

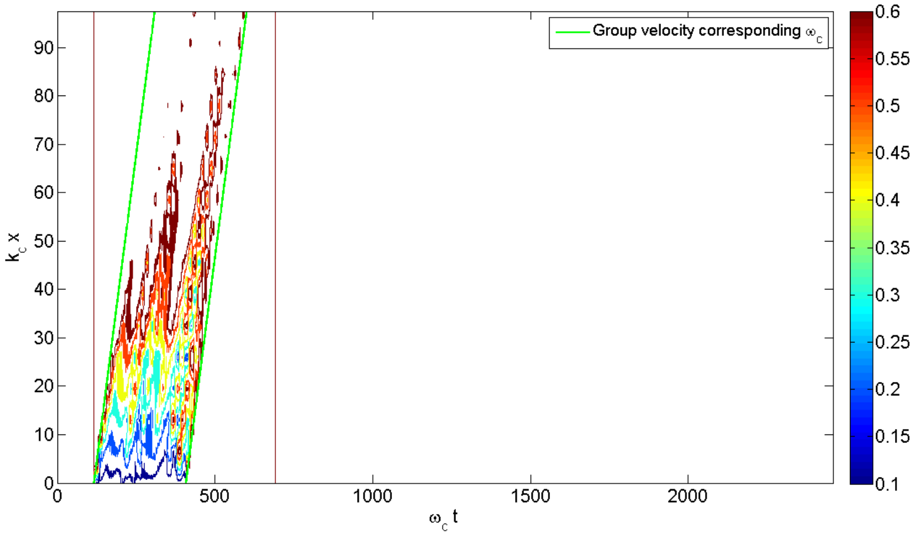

FIGURE 4.17: Normalized space-time error contor along with a bounding line with slope equal to group velocity corresponding to the peak spectrum. 200 realizations are averaged.

Chapter 5

Discussion

5.1 Comments on input data preparation

The quality of measured raw data has a significant impact in deterministic prediction. After thoroughly looking at the treatment of the measured raw data in the simulations so far, different ways may be sought to improve the quality of raw data, specially for the one which will be used to initialize the simulation in deterministic prediction. Evaluation and choice of an initializing time series is essential to validate the models used in the prediction. In this section, the simulations employed so far will be evaluated first. Then, ways that may improve the existing initial time series (at $x = 0$), will be discussed. A comparison with other approaches may also be desirable.

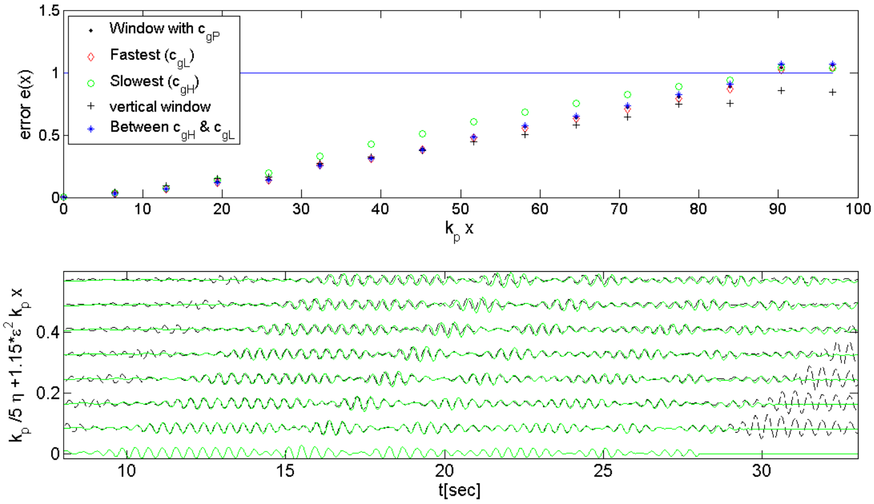

FIGURE 5.1: Upper: Normalized error as a function of normalized distance, it corresponds to the lower plot. Lower: Measured and simulated wave elevation initialized by the time series at x=0, for t $\in [8, 28]s$.

As can be seen in figure 3.2, the time series at the first probe is severely affected by dropouts, specially the groups containing the steepest and highest amplitude waves. In Chapter 3, the handling of missing data and outliers has been discussed. However, it may not give a precise result in deterministic prediction. It only systematically reduces the error associated with interpolation. The negative impact in doing such interpolation is clearly visible by comparing a part of wave groups which are replaced by interpolated data (in figure 3.2) and the corresponding wave groups in figure 4.10. On the other hand, one can use a part of least affected wave groups from the raw data to initialize the simulation. To show this, part of the time series measured at x=0 for t $\in [8, 28]s$, is taken to initialize the simulation. And error graphs, which are similar to those shown in figure 4.8 and 4.9 are plotted in figure 5.1 . The graphs show a significant reduction in error compared to the graphs shown in figure 4.8. However the reduction might also be the result other factors.

As we have seen before, the time series data measured at x=0 is highly contaminated by interpolated data. Let us now start with the second time series data measured at x=0.3m for t $\in [40, 60]s$ to initiate the simulation. The degree of contamination in this time series is some how less, and we expect a better result. The graphs confirm a reduction in error at each probe location than those shown in figure 4.8 of Chapter 4. Comparisons of error graphs from the two cases are also shown in figure B.9.

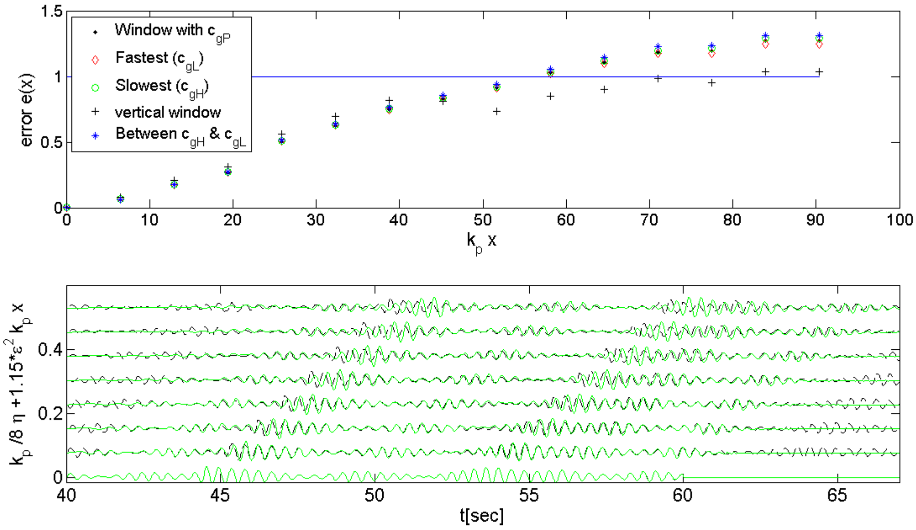

FIGURE 5.2: Upper: Normalized error as a function of normalized distance, it corresponds to the lower plot. Lower: Measured and simulated wave elevation initialized by the time series at x=0.3m, for t $\in [40, 60]s$

5.2 Discussion on results

Experimental measurements are assumed to be perfectly long crested. Therefore equation 2.31, for linear model and NLS equation (2.39), for nonlinear model are employed to simulate the propagation. The NLS equation is reconstructed using second order reconstruction (2.40). In the linear model simulation, the viscous term used damps the waves weakly. Comparisons of simulated and experimentally measured waves within a moving time window are shown in figures 4.7, B.2 and B.3 for linear simulation and in figures 4.15, B.4 and B.5 for NLS simulation.

Linear theory simulation underestimates both phase and group velocities observed in experimentally measured data to some extent. However, the amplitudes observed in the experimental measurements are better estimated in the linear simulation than the NLS simulation.

On the contrary, the NLS simulation better estimates the phase velocity observed in the experimental measurements while it overestimates the amplitudes observed in the experimental measurements. As described by Trulsen [20], the asymmetric forward-leaning evolution observed in the experiments are not seen in the NLS simulation.

A time trace measured at $x = 0$ initialized the simulations, in both the linear and nonlinear models employed in Chapter 4. Most of the results were achieved by taking the worst part of the initializing measured surface elevation. The chosen initializing interval contains a group of waves with steepest and highest amplitude waves. The interval may lead to a larger error but does not change the orientation of the error graphs and contor. This topic is discussed in Section 5.1 to some extent.

For the time trace considered above, the frequency components were computed in Section 4.1.1.2. In the forementioned section, the highest and lowest frequency, phase speed and group velocity components were detailed in table 4.1. The paths of propagation of the input trace, can be represented in a space time diagram as shown in figure 5.3. In deterministic prediction, the space-time diagram has been used by various authors, among them, Morris et al [29], Edgar et al [9] and Naaijen et al [7]. In the diagrams shown in figure 5.3, the input time trace is the base of the triangles bounded by the horizontal axis, the green and blue intersected slanted lines. In each of the graphs, only the area inside the triangle is considered as the predictable zone. Out of the predictable zone, part of a predicted time trace to the left of the vertical line is a hindcast and only the part to right of the vertical line is a forecast. Referring to figure B.10, at any location to the left of the line with slope c_{gH} the shortest wave components observed in the input trace have not arrived yet and at any location to the right of the line with slope c_{gL} the longest wave components found in the input trace have already passed. In

[3], the slopes of the lines used were the phase speed of the shortest and longest wave components of the input trace.

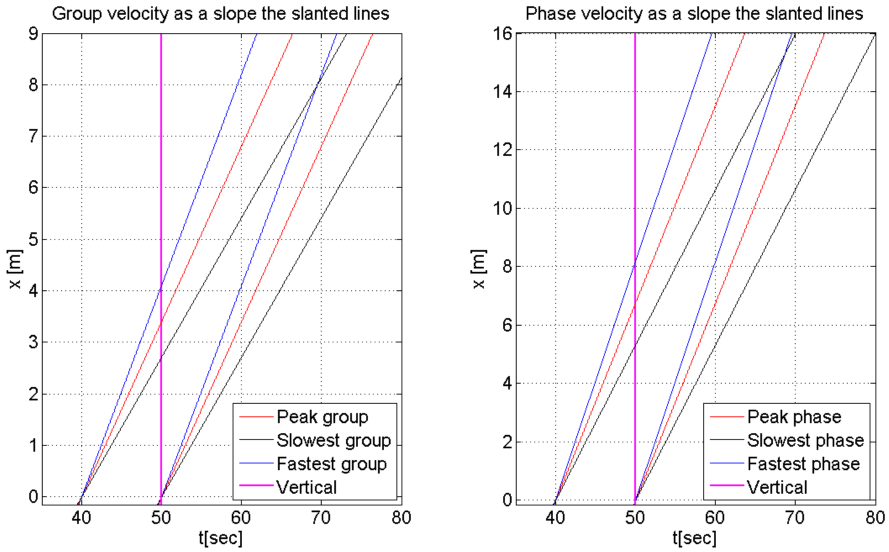

FIGURE 5.3: Propagation lines with slopes equal to group velocity (left) and phase speed (right).

In [1, 3, 9], the slopes of the slanted lines are argued to be determined by the phase speeds $c = dx/dt$, as in figure 5.3 right plot. See [9] for details that favor the phase speed to be the main parameter that bound the predictable area. On the other hand in [6, 7, 30], the slopes of the slanted lines are argued to be determined by the group velocities $c_g = dx/dt$, as shown in figure 5.3 left plot. See [6] for more details that favor the group velocity as the key parameter. In the present study, the main work is, to show that the relevant velocity that bound the prediction region is the group velocity not the phase speed as claimed by the referred article. In the following, the argument from the results achieved in Chapter 4 will be summarized.

From classical hydrodynamic wave theory, it is known that the group velocity for surface gravity waves on deep water is $c_g = \frac{1}{2}c$. If a group of waves are generated on deep water, then the generated waves will propagate at a speed of c_g, which implies that the waves will propagate up to half of the distance expected by the phase speed. Therefore the wave amplitude will be zero at the leading and trailing edges of the group and thus the group velocity is the speed of propagation of energy. It implies that there are no waves in the domain $x \in (\frac{1}{2}ct, ct]$.

The energy density is directly proportional to the square of the surface elevation as presented in Section 2.1.1. This suggests that, the error criterion (4.6) and (4.7) have close relation to the energy density through the surface elevation involved in the equations. Therefore, the energy density is the norm to calculate the prediction error which in turn favors the group velocity as the parameter bounding the prediction area. See Section 2.1.1 concerning the relationship between the energy density and the group velocity.

Consider again that, the time trace measured at $x = 0$, for t $\in [40, 60]$ initializes the propagation of the wave. At any point in space for $x > 0$, the propagation of the input trace measured at $x = 0$ will look like the one shown in figure 4.10, for linear model and figure B.7, for nonlinear model. The prediction error is calculated by using equation 4.7. The error contors (4.11) and (4.17) resulted from equation 4.7, show that the error increases gradually from 0 inside the bounded region to 1 near the boundaries of the contor plot. Outside the boundaries, the error becomes larger than one. On the same plot, two lines are shown on both sides of the contor. The lines have a slope equal to the group velocity (c_{gP}), corresponding to the peak frequency. The edges on both sides of the contor plot coincide with the lines with slope c_{gP}. This shows that, only the region inside the two bounding lines is predictable. Therefore, the group velocity is the relevant parameter that bound the prediction region. On the contor plot (B.8), The error value $e = 1$, does not coincide with the lines with slope c_{gP}. Therefore another line with a slope equal to the fastest group velocity (c_{gL}), is shown on the right side of the contor. This time the line almost coincides with the contor $e = 1$. And a line with a slope equal to the slowest group velocity (c_{gH}), is shown on the left side of the contor. The contor $e = 1$ on the left side of the contor is not clearly visible for comparison.

Chapter 6

Conclusion and Suggestions for further works

6.1 Conclusion

In this thesis, we have investigated the relevant parmeter that determine the prediction region deterministically for long-crested waves. The deterministic prediction of the waves is carried out by first initializing the models with experimental measurement. The measurement taken at the first probe is used to initialize the propagation model. Two models have been employed to simulate the shape of the waves at different probe locations downstream of the wave tank. Then the experimental measurements taken at different probes are used to control the precession of theoretically predicted waves at the respective probe locations.

Apart from dropouts present in the data, the experimental measurements are generally good. In the simulation, the chosen time interval in the time series is affected by the dropouts. However parallel simulation has been done with least affected time interval to control the simulation. The dropouts have been replaced by interpolated data.

Linear and weakly nonlinear wave propagation models have been used. The linear model takes surface tension and viscous damping into account on arbitrarily deep water. The model is derived from the linear wave theory. The weakly nonlinear model is simulated for gravity waves on deep water. The model is derived from Schrödinger equation. Then the NLS equation is implemented with second order reconstruction of the surface elevation.

The two models yield similar result but the linear model performed better generally. The wave amplitudes are predicted better by linear theory than NLS model. While, the phase and group velocities predicted better by NLS than linear theory model. The normalized error is larger for the NLS case. The reason for larger error for NLS is that, the amplitudes of the waves are overestimated, in addition, the trailing side of the wave group is not correctly predicted and the third reason may be referred in paragraph 4.2.1.3. For normalized error $e \in [0, 0.6]$, the two models are almost comparable. For simulation, with time interval that contain smaller amplitude wave group, the NLS performed better. In this case the two models resulted in almost equal prediction at each of the probe locations.

The propagation of the waves are predicted and the models used are tested by available experimental data so far in the conclusion. The next will be the determination of the pertinent parameter which bound the prediction region. The thesis, focuses on the argument that the group velocity is the pertinent parameter that bound the prediction region. We know that, the group velocity is favored by the energy density. Then the benefit from the energy density can be used by setting it as the norm to calculate the prediction error.

A suitable time interval is first chosen, to initialize the simulation. Then the prediction error, whose norm is the energy density, is calculated in space and time. The resulting contor plot shows that, the error starts from zero, near the first probe, and increases gradually to one, near both sides of time interval and far downstream. Bounding lines with slope equal to c_{gP} plotted on both sides of the contor. The error outside of the bounding lines is observed to be larger than one showing that, the group velocity is the relevant parameter which bound the prediction area.

The inclination of the right edge of the contor with error $= 1$, coincides to some extent with the fastest group velocity. While it is not clearly visible on the left edge of the contor. The time interval chosen is large such that, the lines with slopes equal to the slowest and fastest group velocities do not intersect within the limit of the last probe location. Besides, the relevant contor plot (B.8), is a result of only 1000 realizations. Therefore, it becomes difficult to draw a clear conclusion on the dependence of the predictable area on the fastest and slowest group velocities. However, the orientation of the left and right edges of contor plot look like the orientation of the slowest and fastest velocities respectively.

As discussed earlier, the right and left boundaries of the space-time prediction error contor coincide with the lines with slope equal to the group velocity corresponding to the peak spectrum. The two lines limit the prediction region. The region outside the two boundaries is totally unpredictable as the waves contained in the input trace have not arrived the outer region. Therefore, the group velocity is the relevant parameter that bounds the prediction region not the phase speed as claimed in [9].

6.2 Suggestions for further works

In the beginning, a number of questions were planned to be answered in this thesis. Moreover, many interesting questions arose during the study. However, due to short time available some of the questions are not answered in this thesis. The questions will be proposed for further works as follows:

Long crested waves using MNLS model: Others work suggested that the MNLS model give a very good result in deterministic prediction. Therefore using such models can give a more precise result. The results can be used as a fine-tuning for the models done in the thesis. Furthermore, the prediction region and predictable area may clearly be visible.

Short crested waves using linear and nonlinear models: In reality ocean waves are not perfectly long crested. Therefore doing such models on short crested waves will give a more realistic result and conclusion.

Use other norms which favors phase speed: This may help to see whether other norms may result in the same conclusion or not.

Appendix A

Solving the boundary value problem for linear wave

A.1 Derivation of velocity potential, dispersion relation and velocity components

The Laplace equation (2.1) can be written as

$$\frac{\partial^2\phi}{\partial x^2}+\frac{\partial^2\phi}{\partial z^2}=0. \tag{A.1}$$

We seek a solution of the form

$$\phi=f(z)\sin(kx-\omega t)=f(z)e^{-ikx+i\omega t)}. \tag{A.2}$$

(A.2), (2.8) and (2.9) into (A.1) give

$$f''-k^2f=0, \quad for \quad -H<z<0, \tag{A.3}$$

$$-\omega^2f+gf'+\frac{\sigma}{\rho}k^2f'=0, \quad \text{at} \quad z=0, \tag{A.4}$$

$$f'=0, \quad at \quad z=-H. \tag{A.5}$$

The solution to A.3 with the condition A.5 gives

$$f(z) = A\cosh k(z+H), \quad \text{at} \quad z = -H. \tag{A.6}$$

(A.6) into (A.2) gives

$$\phi = A\cosh k(z+H)e^{-ikx+i\omega t}, \quad \text{for} \quad z = -H, \tag{A.7}$$

where A is an arbitrary constant. Equation A.7 satisfied only if

$$\omega^2 = (gk + \frac{\sigma}{\rho}k^3)\tanh kH. \tag{A.8}$$

Substitution of (A.7) and (2.10) into (2.7) and evaluating the $\frac{\partial\phi}{\partial z}$ at $z = 0$ we get

$$\frac{\partial\eta}{\partial t} = Ak\sinh(kH)e^{-ikx+i\omega t}, \tag{A.9}$$

integration results in

$$\eta = i\omega a e^{-ikx+i\omega t} = Ak\sinh(kH)e^{-ikx+i\omega t}. \tag{A.10}$$

The constant A is then

$$A = \frac{i\omega a}{k\sinh kH}. \tag{A.11}$$

Upon substitution the constant A and the dispersion relation (A.7) gives the desired solution

$$\phi = \frac{-iga}{\omega}\left(1 + \frac{\sigma k^2}{g\rho}\right)\frac{\cosh k(z+H)}{\cosh kH}e^{-ikx+i\omega t}. \tag{A.12}$$

Derivation of the velocity potential with respect to x and z gives the velocity field

$$u = \frac{gak}{\omega}\left(1 + \frac{\sigma k^2}{g\rho}\right)\frac{\cosh k(z+H)}{\cosh kH}e^{-ikx+i\omega t}, \tag{A.13}$$

and

$$w = \frac{-igak}{\omega}\left(1 + \frac{\sigma k^2}{g\rho}\right)\frac{\sinh k(z+H)}{\cosh kH}e^{-ikx+i\omega t}. \tag{A.14}$$

Appendix B

Some figures from results and numerical iteration method

B.1 Smoothing

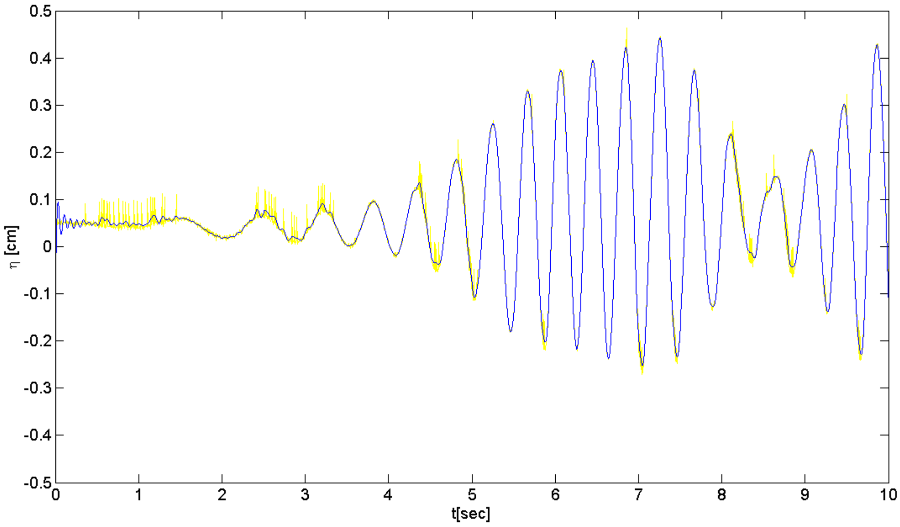

FIGURE B.1: Typical time series before and after smoothing.

B.2 Numerical iteration to determine wavenumber

ω_j is known

start with dispersion relation for infinite depth

$$k_{j,0} = \frac{\omega_j^2}{g}, \tag{B.1}$$

$$k_{j,1} = \frac{\omega_j^2}{(g + \frac{\sigma k_{j,0}^2}{\rho})\tanh(k_{j,0}h)}, \tag{B.2}$$

$$\begin{aligned} k_{j,2} &= \frac{\omega_j^2}{(g+\frac{\sigma k_{j,1}^2}{\rho})\tanh(k_{j,1}h)}, \\ &\vdots \\ &\vdots \\ &\vdots \end{aligned} \tag{B.3}$$

$$k_{j,J} = \frac{\omega_j^2}{(g + \frac{\sigma k_{j,J-1}^2}{\rho})\tanh(k_{j,J-1}h)}, \tag{B.4}$$

converges if $\left|\frac{d}{dk}\left(\frac{\omega^2}{(g+\frac{\sigma k^2}{\rho})\tanh(kh)}\right)\right| < 1$.

B.3 A comparison of measured and simulated (by linear model) surface elevation for probes 5 to 16

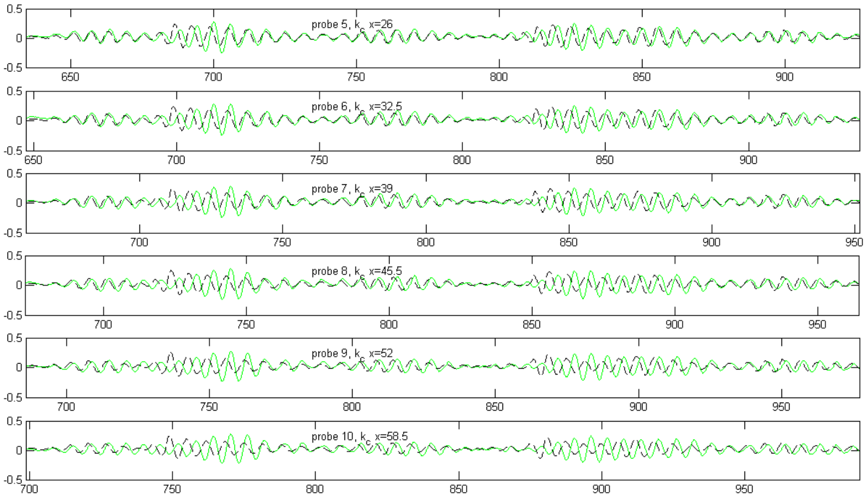

Figure B.2: Measured and simulated (green solid curves) time series at probes 5 through 10.

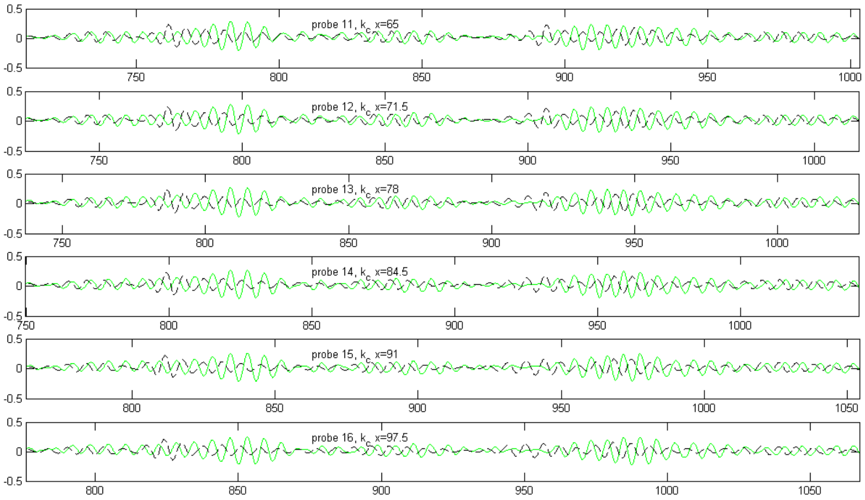

Figure B.3: measured and simulated (green solid curves) time series at probes 11 through 16.

B.4 A comparison of measured and NLS simulated surface elevation for probes 5 to 16

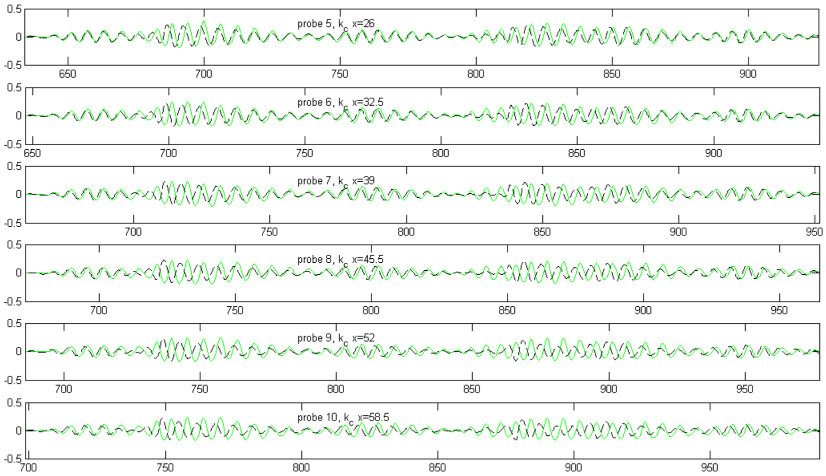

Figure B.4: Measured (dashed curves) and NLS predicted (green solid curves) surface elevation for probes 5 to 10.

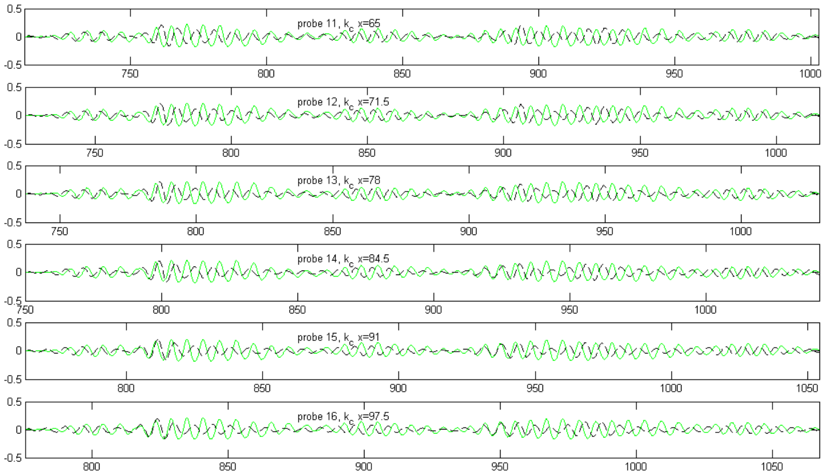

Figure B.5: Measured (dashed curves) and NLS predicted (green solid curves) surface elevation for probes 11 to 16.

B.5 Additional figures

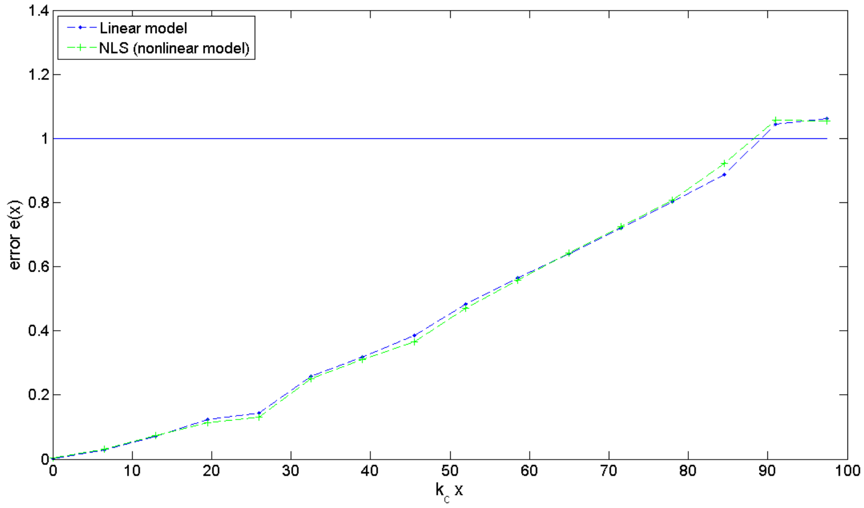

FIGURE B.6: Normalized error for linear and NLS simulation. The simulation is initialized by time series at $x = 0$ for t $\in [8, 28]s$

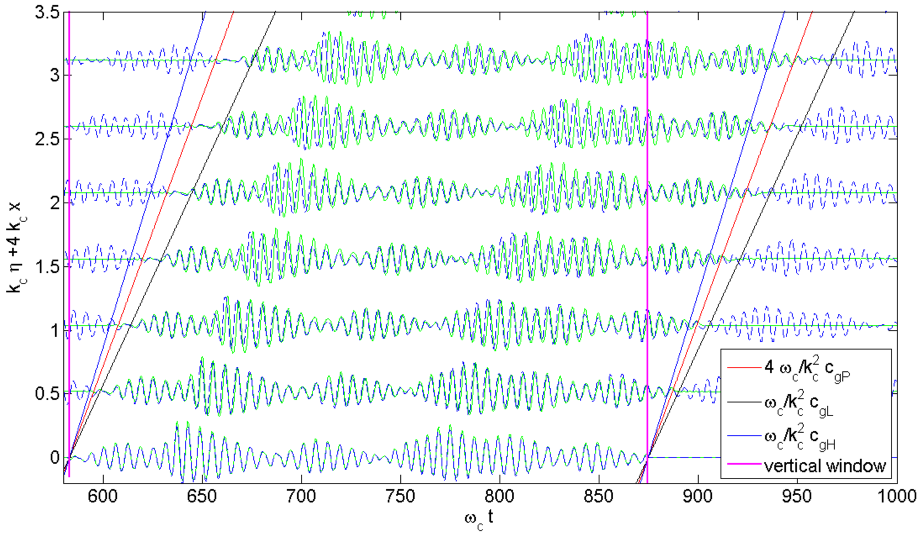

FIGURE B.7: Measured and NLS simulated time series for one realization for probes one through seven.

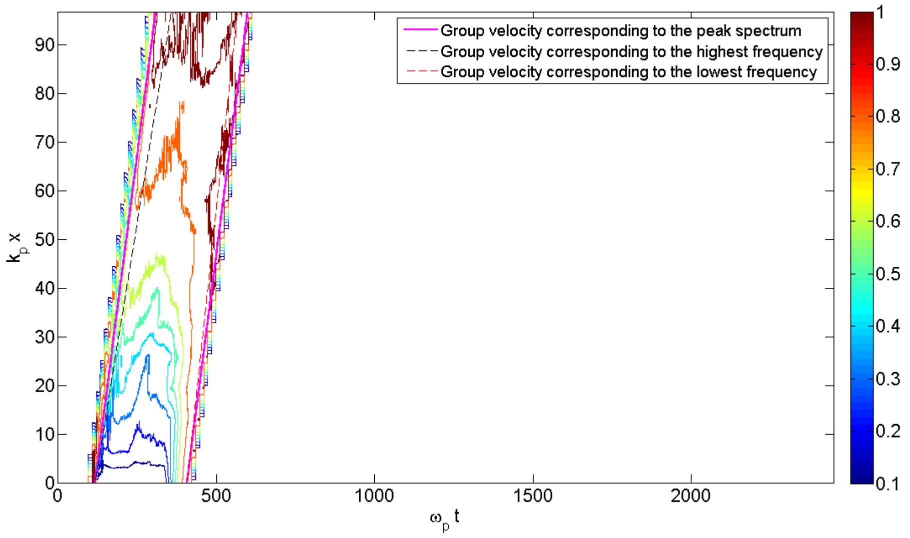

FIGURE B.8: Normalized space-time error contor along with a bounding line with slope equal to group velocity corresponding to the peak spectrum, slowest and fastest group velocity. 1000 realizations are averaged.

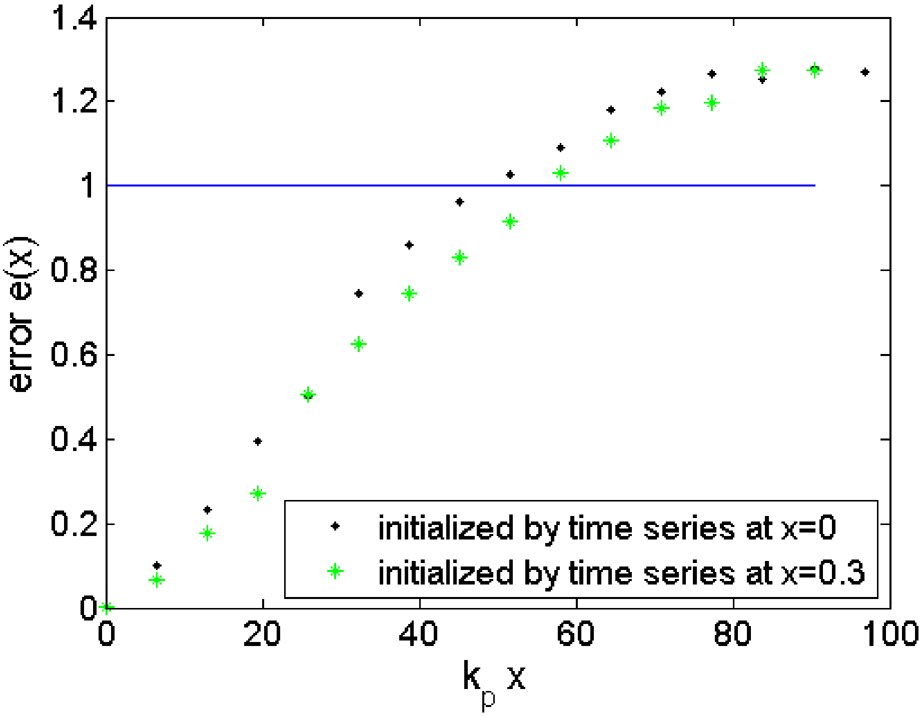

FIGURE B.9: Normalized error as a function of normalized distance. Initialized by the time series at $x = 0$ and $x = 0.3$ for $t \in [40, 60]s$.

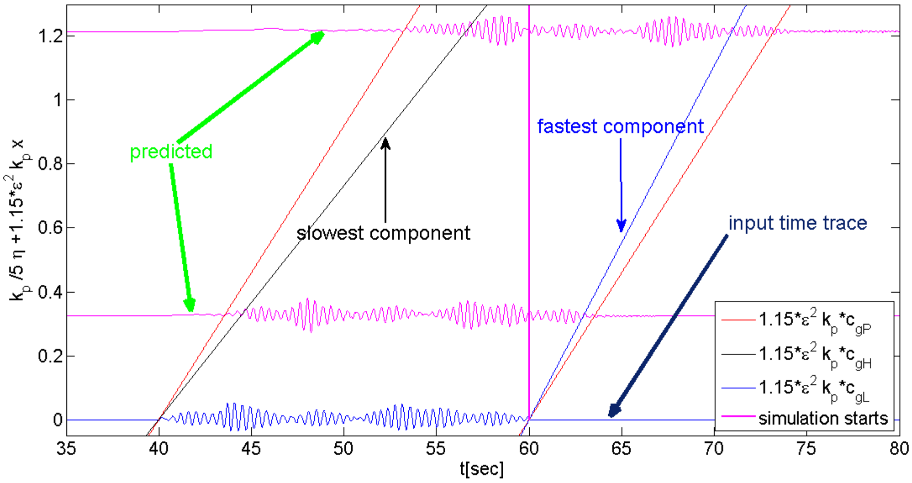

FIGURE B.10: Propagation of the input trace measured at $x = 0$, represented in a space-time diagram.

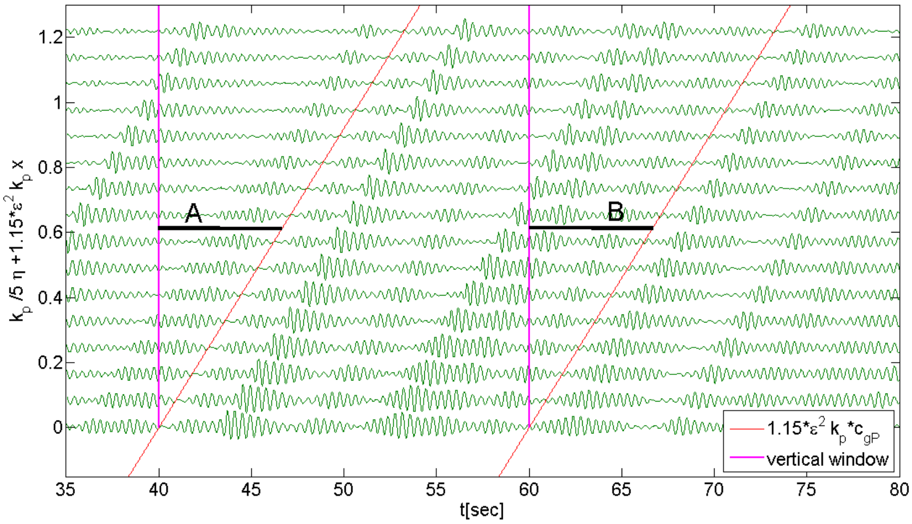

FIGURE B.11: Property of the normalized error within the vertical window.

Appendix C

Numerical method for NLS equation

C.1 Split-step pseudo-spectral method

As already said in section 4.2.1.2, the linear and nonlinear terms of the cubic Schrödinger (4.17) are treated separately. Let us write equation 4.18, with N replaced by Q as follows:

$$\frac{\partial B}{\partial x} = L(B) + Q(B). \tag{C.1}$$

The nonlinear part is

$$\frac{\partial B}{\partial x} = -Q(B), \tag{C.2}$$

$$where \qquad Q(B) = i|B|^2 B. \tag{C.3}$$

Where as the linear part is

$$\frac{\partial B}{\partial x} = -L(B), \tag{C.4}$$

$$where \qquad L(B) = 2\frac{\partial B}{\partial t} + i\frac{\partial^2 B}{\partial t^2}. \tag{C.5}$$

Equation C.2, is solved for B using a midpoint finite difference approximation. The nonlinear term (C.3) is calculated as follows

First calculate $\hat{B}(t, x + \frac{1}{2}\Delta x)$ using a forward difference

$$\hat{B}(t, x + \frac{1}{2}\Delta x) = B(t, x) - \frac{1}{2}\Delta x Q(B(t, x)), \tag{C.6}$$

Let $\hat{\hat{B}}(t, x + \Delta x)$ be a solution to (C.2), then

$$\hat{\hat{B}}(t, x + \Delta x) = B(t, x) - \Delta x Q(\hat{B}(t, x + \frac{1}{2}\Delta x)). \tag{C.7}$$

The linear part involves

$$\frac{\partial B}{\partial x} + 2\frac{\partial B}{\partial t} + i\frac{\partial^2 B}{\partial t^2} = 0. \tag{C.8}$$

The Fourier transform of (C.8) is

$$\frac{\partial \hat{B}}{\partial x} = -i(2\omega - \omega^2)\hat{B}, \tag{C.9}$$

then the exact solution to (C.9) is

$$\hat{B}(\omega, x) = \hat{B}(\omega, 0)e^{-i(2\omega-\omega^2)x}. \tag{C.10}$$

$\hat{B}(\omega, 0)$ can be determined from initial condition as $\hat{B}(\omega, 0) = F\left[B(t, 0)\right]$ at $x = 0$. The analytic solution of the linear part in Fourier domain is

$$\hat{B}(\omega, x) = \hat{B}(\omega, 0)e^{-i(2\omega-\omega^2)x}. \tag{C.11}$$

Finally the numerical solution at each spatial step $B(t, x+\Delta x)$ is computed by combining $\hat{\hat{B}}(t, x + \Delta x)$ and (C.11) in the following manner

$$B(t, x + \Delta x) = F^{-1}\left[F\left[\hat{\hat{B}}(t, x + \Delta x)\right]e^{-i(2\omega-\omega^2)\Delta x}\right]. \tag{C.12}$$

This completes the derivation of 4.19.

Bibliography

[1] D. R. Edgar, J. M. K. Horwood, R. Thurley, and M. R. Belmont. The effects of parameters on the maximum prediction time possible in short term forecasting of the sea surface shape. *International Shipbuilding Progress*, 47(4511):287–301, 2000.

[2] H. Johnsgard and E. Gjølmesli. A brief summary of marine operations and engineering. MEK 4450, DNVkvarnær module, 2011.

[3] P. Naaijen and R. Huijsmans. Real time wave forecasting for real time ship motion prediction. *Proc. twentyseventh Intl Offshore Mechanics and Arctic Engineering*, OMAE2008-57804(28):1–8, 2008.

[4] K. Trulsen. Weakly nonlinear sea surface waves, freak waves and deterministic forecasting. *SINTEF Applied Mathematics*, (12):191–209, 2006.

[5] K. Trulsen. Simulating the spatial evolution of a measured time series of a freak wave. *In Michel Olgnon, Gerassimos Athanassoulis*, Rogue waves 2000:265–273, 2001.

[6] G. Wu. Direct simulation and deterministic prediction of large-scale nonlinear ocean wave-field. *PhD Thesis, M.I.T*, 2004.

[7] P. Naaijen, R. van Dijk, R. M. M. Huijsmans, A. A. El-Mouhandiz, and J. Danneberg. Real time estimation of ship motions in short crested seas. *Proc. twenty eighth Intl Offshore Mechanics and Arctic Engineering*, OMAE2009-79366(28):1–13, 2009.

[8] M. Cohen P. K. Kundu. *Fluid Mechanics.* Academic Press, 4 edition, 2008.

[9] C. Abusedra and M. R. Belmont. Prediction diagrams for deterministic sea wave prediction and the introduction of the data extension prediction method. *International Shipbuilding Progress*, 58(58):59–81, 2011.

[10] G. B. Whitham. *Linear and nonlinear waves.* John Wiley and Sons, Inc., a wiley-interscience series of texts, monographs, and tracts edition, 1974.

[11] B. Gjevik, G. K. Pedersen, and K. Trulsen. Hydrodynamic wave theory. MEK 4320, Lecture notes, 2010.

[12] H. Lamb. *Hydrodynamics.* Cambridge University Press, sixth edition, 1932.

[13] J. C. Padrino and D. D. Joseph. Correction of Lamb's dissipation calculation for the effects of viscosity on capillary-gravity waves. *Physics of fluids*, DOI-10.1063/1.2760244(19):082105–1–082105–6, 2007.

[14] J. Billingham and A. C. King. *Wave Motion.* Cambridge University Press, cambridge texts in applied mathematics edition, 2000.

[15] J. N. Newman. *Marine Hydrodynamics.* The MIT Press, isbn 978-0-262-14026-3 edition, 1977.

[16] K. Trulsen, I. Kliakhandler, K. B. Dysthe, and M. G. Velarde. On weakly nonlinear modulation of waves on deep water. *Phy. Fluids*, 12,2432; doi:10.1063/1.1287856: 2432–2437, 2000.

[17] H. E. Krogstad and K. Trulsen. Interpretations and observations of ocean wave spectra. *Ocean Dynamics (2010) 60:973-991*, DOI 10.1007/s10236-010-0293-3:973–991, 2010.

[18] K. B. Dysthe. Note on a modification to the nonlinear Schrödinger equation for application to deep water waves. *Proc. R. Soc. Lond A*, 369(1736):105–114, 1979.

[19] K. Trulsen. Real time deterministic ocean wave forecasting using weakly nonlinear wave evolution. *App. Mathematics SINTEF*, MekiT'03:371–390, 2003.

[20] K. Trulsen. Spatial evolution of water surface waves: Numerical simulation and experiment of bichromatic waves. *SINTEF Applied Mathematics*, III(ISBN 1-880653-54-0):71–77, 2001.

[21] T. M. A. Taklo. How well is the linear dispersion relation satisfied for laboratory waves. Master's thesis, Universitetet i Oslo, 2012.

[22] *Matlab data analysis.* Math works inc., 2005. URL `http://cda.psych.uiuc.edu/matlab_class_material/data_analysis.pdf`.

[23] E. Lo and C. Mei. A numerical study of water-wave modulation based on a higher-order nonlinear Schrödinger equation. *J. Fluid Mech.*, 150:395–416, 1985.

[24] Y. Zhang and R. Li. Numerical solutions for two nonlinear wave equations. *Water science and Engineering*, doi:10.38882/j.issn.1674-2370.2012.04.005:410–418, 2012.

[25] T. R. Taha and M. J. Ablowitz. Analytical and numerical aspects of certain nonlinear evolution equations. II. Numerical, nonlinear Schrödinger equation. *Journal of computational physics.*, 55:203–230, 1984.

[26] G. H. Weiss and A. A. Maradudin. The Baker-Hausdorff formula and a problem in crystal physics. *J. Math. Phys.*, 3:771–777, 1962. URL `http://dx.doi.org/10.1063/1.1724280`.

[27] G. P. Agrawal. *Nonlinear fiber optics.* Academic Press, 4th edition edition, 2007.

[28] G. M. Muslu and H. A. Erbay. Higher-order split-step Fourier schemes for the generalized nonlinear Schrödinger equation. *Mathematics and Computers in simulation.*, 67:581–595, 2004.

[29] E. L. Morris, H. K. Zienkiewicz, and M. R. Belmont. Short term forecasting of the sea surface shape. *International Shipbuilding Progress*, 45(444):383–400, 1998.

[30] J. Dannenberg, P. Naaijen, K. Hessner, H. v. d. Boom, and K. Reichert. The on board wave and motion estimator. *OceanWaveS, GmbH, TU Delf, MARIN and OceanWaves Pacific*, OMAE:1–8, 2010.